ABSTRACT

Title of Document: DEVELOPMENT OF A TEST METHODOLOGY TO DETERMINE DYNAMIC FRACTURE STRENGTH IN MICROFABRICATED MEMS STRUCTURES

Rachel Lauren Emmel, M.S. Engineering, 2009

Directed By: Professor Donald Barker, Department of Mechanical Engineering

As micro-electro-mechanical systems (MEMS) are becoming more and more common in both military and consumer electronics, virtual qualification of these devices remains an important design tool. To model MEMS devices subjected to high shock loading, the dynamic fracture strength of the most widely used MEMS material, single crystal silicon (SCSi), is needed. Minimal research has been performed to determine this material property and the research that has been completed suggests that fracture strength varies considerably with processing parameters. Therefore, an efficient and inexpensive testing method to determine the dynamic fracture strength of processed SCSi has been developed.

Experimentation with SCSi MEMS structures has also been carried out using this new testing method. A probabilistic Weibull distribution for bending of DRIE processed SCSi around the <110> directions was created as a design for reliability tool. Additional experiments demonstrated that the fracture strength for bending of DRIE processed SCSi around the <100> directions is greater than 1.1 GPa. Suggestions for subsequent work that focuses on the bending of SCSi around the <100> directions are also presented.

DEVELOPMENT OF A TEST METHODOLOGY TO DETERMINE DYNAMIC FRACTURE STRENGTH IN MICROFABRICATED MEMS STRUCTURES

By

Rachel Lauren Emmel

Thesis submitted to the Faculty of the Graduate School of the
University of Maryland, College Park, in partial fulfillment
of the requirements for the degree of
Master of Science in
Mechanical Engineering
2009

Advisory Committee:
Professor Dr. Barker, Chair
Professor Dr. McCluskey
Professor Dr. Sarah Bergbreiter

Dedication

To Tim and Scruff McGruff.

Acknowledgements

I would like to thank:

- Dr. Donald Barker, for his very practical advice and guidance on this project
- My mom, dad, and brother, David, for their love and support throughout all the years of my undergraduate and graduate studies
- Saifa Hasin for her contributions to this project as a co-investigator
- "Team Barker," especially Gil, Patrice, and Jamie for the endless stream of brownies and cookies, the sunny day lunchtime outings, and all of the ridiculous conversation. Thanks to you guys, there has never been a dull moment in this office.
- Dr. Nathan Blattau of DfR Solutions and Mr. Morris Berman of the US Army Research Laboratory for providing access to the some of the drop tower systems used in this research
- QinetiQ, for designing and fabricating the MEMS test structures

Table of Contents

List of Tables

List of Figures

Chapter 1: Introduction

It is well known that the development of microelectromechanical systems (MEMS) is revolutionizing the modern consumer and military electronics industries. The incorporation of both electrical and mechanical functionality into a small, micro-scale package has both reliability and cost benefits that are being exploited in many products today. In fact, MEMS are found everywhere from smart munitions to inkjet printers. They are used as accelerometers for airbag deployment and for Nintendo Wi game controllers, pressure sensors for vehicle tires and blood pressure monitoring, gyroscopes, optical switches, displays, biomolecule sensors, chemical sensors, and many more systems requiring dual sensing and actuation. Yole Développement, a French company that focuses on semiconductor, optics, microfluidics, and MEMS market research, generated the predictive market chart shown below in Figure 1 [1].

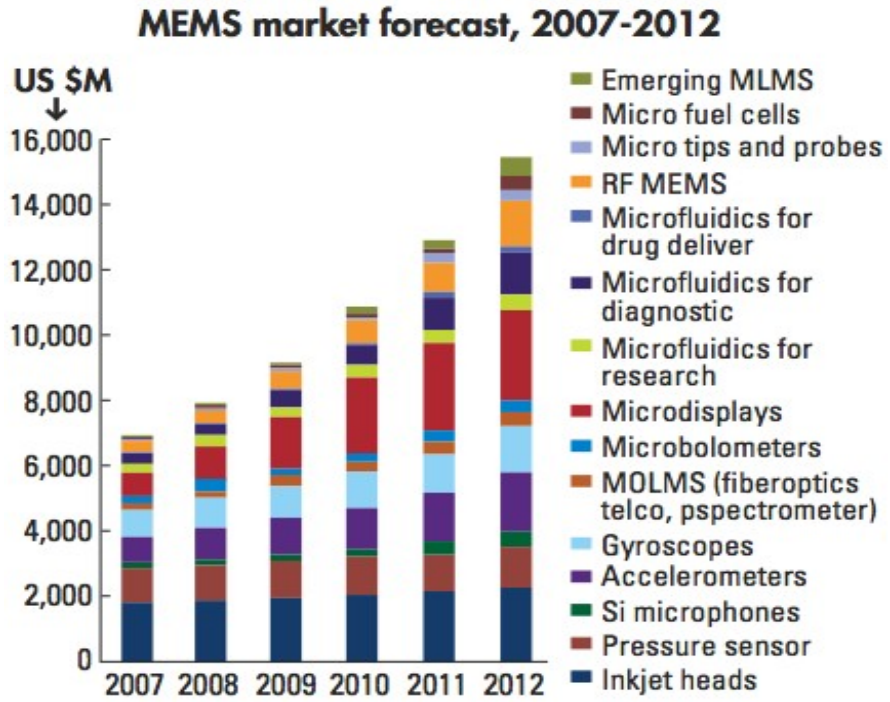

Figure 1. Predictive chart of MEMS trends through 2012 [1]

The chart above shows not only exceptional growth in MEMS development through 2012 but also demonstrates industry trends. Growth of RF MEMS, micro fuel cells, and various medical devices is particularly evident.

Figure 1 above shows that many MEMS devices are being designed into common household, medical, industrial, and military devices. The reasons for the incorporation of MEMS include both increased performance and decreased cost. However, the majority of product-level testing of these devices is through experimentation [2]. Not only are pass/fail validation tests costly and time consuming, but they also cannot account for the wide variation in use of products. An ideal design strategy to minimize the need for costly testing is the implementation of modeling and virtual qualification. This strategy requires well documented mechanical properties of materials used in the devices of interest. Single Crystal Silicon has traditionally been viewed as the primary building block for MEMS devices and fortunately, many of its mechanical properties are well documented.

Because MEMS are being incorporated into many devices that experience high shock loading such as gun launched munitions, cell phones, mp3 players, and medical devices, virtual qualification of these products in high acceleration environments is necessary. To accurately model such conditions, dynamic fracture strength values for materials common in MEMS devices are required. Unfortunately, although tremendous research has been performed on the static fracture strength of single crystal silicon to determine how various processing techniques affect it, very

little work has been performed to determine the dynamic fracture strength of single crystal silicon.

In order to enable virtual qualification of MEMS structures subjected to high shock loading, the dynamic fracture strength of single crystal silicon is required. Therefore, this research focuses on establishing an expedient and inexpensive methodology to determine dynamic fracture strength. A second goal of this project is to validate this method by subjecting simple shock test structures to high accelerations though the use of a drop tower. The results of this research will tremendously aid in MEMS designers' ability to use modeling and virtual qualification instead of costly and time consuming pass/fail testing for both military and consumer products.

Chapter 2: Literature Review

Introduction

As MEMS devices become increasingly common in commercial and military systems, the need for accurate mechanical property values of single crystal silicon is increasing as well. Therefore, an enormous quantity of research in this area has taken place in the last decade. Unfortunately, however, characterizing the mechanical properties of single crystal silicon for MEMS devices presents a number of unique challenges.

The first of these challenges is that single crystal silicon is typically formed into small, microscale features when used in functional devices. Ideally, mechanical property testing is performed on structures of the same size scale to ensure that the data being gathered is representative of the single crystal silicon found in MEMS devices. However, standard mechanical property characterization tests such as tensile testing, fatigue testing, and fracture toughness testing are challenging to implement on such small specimens. Therefore, these previously developed tests must be modified or new tests must be developed in order to determine mechanical properties of MEMS materials through experimentation. Examples of the alternative test methods that have been implemented for small scale structures include membrane-bulge tests, beam-bending tests, and frequency response tests have been used [3].

Another challenge associated with mechanical testing stems from the fact that single crystal silicon can be processed using a number of different techniques. Each of these techniques leaves various sized defects and surface roughnesses that have

been demonstrated to influence material properties such as fracture strength [4]. In addition to the variability in the type, prevalence, and size of these etching defects, there is also large variability in how much of an effect these defects have on test samples. The effect of these defects on mechanical properties is often suggested to scale with the geometry of the sample being tested. For example, a 1µm defect in a a mesoscale structure with dimensions in the 0.1-10mm range may not have as dramatic an impact as the same defect in a microscale structure with dimensions in the 0.1-100µm range. This reality emphasizes the importance that researchers must place on documentation of both test structure geometries and processing techniques when publishing their test data. Without this information it is challenging, if not impossible, to gain meaningful insight by comparing one mechanical property study to another.

The anisotropic crystal structure of single crystal silicon also introduces some variability in test data. There are three primary cleavage planes in single crystal silicon: {100}, {110}, and {111}. It has been observed that the fracture path that appears during testing varies with the loading direction relative to the three cleavage planes as well as the velocity of crack propagation [5]. In turn, the fracture path, or cleavage plane, strongly influences the fracture strength of the test sample. Fracture strength is formally defined as the "level of stress at the highest stressed location in the structure at the instant of rupture" [6]. Wilson and Beck provided experimental results that identified the {111} plane as the weakest plane in single crystal silicon. This result is consistent with common knowledge regarding the crystal structure of the material. In their work, Wilson and Beck also found that the fracture strength was

1.3 GPa for cracks along the {111} plane and 2.3 GPa for cracks along the {110} plane [5]. However, there is still wide variability in fracture strength data and its dependence on crystal orientation.

Despite the challenges discussed above, a significant amount of work is being performed to determine the mechanical properties of single crystal silicon and to relate the variability in these values to different processing techniques. Because single crystal silicon is a brittle material and has no yield point, its ultimate strength is the same as its fracture strength and represents the stress value at which the material fails. Therefore, fracture strength is a beneficial metric for device designers who work with single crystal silicon.

Test Method Deveopment for Miscroscale Structures

To mitigate some of the difficulties associated with mechanical testing of single crystal silicon MEMS structures, many novel test methods have been developed. There are two primary testing techniques that have been extensively performed on single crystal silicon structures. Microscale tension testing, as with macroscale testing, has been used to directly measure Young's Modulus, fracture strength, and Poisson's ratio [3]. Bend testing, on the other hand, has been used primarily to indirectly determine fracture strength. It is important to note that microscale tension testing typically involves a more complicated setup because it requires accurate alignment of the sample, fixed sample ends, a deflection measurement technique, and a larger applied force than bend testing [3]. Tension testing does, however, provide more reliable measurements as well as Young's

modulus and Poisson's ratio values [3]. This section describes some of the methods researchers have used to overcome the obstacles associated with testing microscale structures.

One of the difficulties in creating test samples for a single crystal silicon tensile test is that high aspect ratio structures are often hard to generate through standard etching techniques. However, a team from the NASA Glen Research Center demonstrated that simple microtensile specimens could be fabricated [6]. Nemeth et al. determined that a highly directional deep reactive ion etching (DRIE) process was optimal for creating these structures because of its ability to control sample strength, surface finish, and other important properties [6].

Another problem with MEMS tensile testing is that due to the small size scale, it is challenging to find a method to secure the specimens for testing without damaging them. Traditional tensile testing requires the test specimen to be fixed at each end. Such a setup, however, is not easy to implement with microtensile specimens. Yi and Kim developed a uniaxial tension testing method that mitigates this problem. Instead of applying a force through direct physical contact, this method uses a Lead Zirconate Titanate (PZT) actuator that functions using the piezoelectric effect [7]. The PZT actuator described above elongates the test specimen when a voltage is applied [7]. The force applied is measured by a load cell and the resultant strain is determined through optical interferometry [7]. This test method eliminates the need for any physical handling of the microbeam to ensure that it is not damaged or compromised in any way prior to testing. Results of Yi and Kim's tests are discussed in the following section.

To sidestep the problems and challenges associated with microscale tensile testing, Namazu et al. determined a bend testing method to examine the effect of size scale on the mechanical properties of single crystal silicon. To test size scale effects, six different sized beams with widths of 0.2µm to 1800µ, thicknesses of 0.255µm to 520µm, and lengths of 6µm to 9850µm, were prepared [8]. A diamond tip attached to a cantilever was used to deflect the beams in the bend tests [8]. To determine the deflection of the cantilever, a PZT actuator was employed. Unlike the PZT actuator used by Yi and Kim, this actuator effectively operates in reverse and operates on the principle of the piezoelectric effect to measure resultant voltage when the cantilever is deflected. Subsequent linear elastic theory calculations allowed Namazu et al. to determine both young's modulus and bending strength. They found that size scale did not have a significant impact on Young's Modulus but that it did indeed influence bending strength [8]. Their results demonstrated that as specimen size decreases, bending strength increases. Examination of the fracture surfaces later revealed that the discrepancy in strength stems from differences in crack initiation sites [9]. This is an interesting phenomenon that suggests VLSI and MEMS designers may require multiple single crystal silicon mechanical property values to fully characterize devices which incorporate a wide range of structure sizes.

Etchant Effect on Fracture Strength

The availability and widespread use of a large range of etchants has sparked interest in their effects on the mechanical properties of silicon. Many investigations focusing on the relationship between fracture strength and surface roughness, surface

finishes, and directionality of etchants have been performed [7] [10] [11] [12]. The results of some of these investigations are discussed below.

Many groups have attempted to determine the quasi-static fracture strength of silicon wafers prior to microfabrication steps. Hu demonstrated the effect of various wafer polishing techniques and different overlay materials on fracture strength. He found that silicon wafers polished with silica gel had an average fracture strength of 2.8 GPa, while mechanically lapped surfaces with some defects penetrating deeper than 3µm had an average fracture strength of only 0.3-0.4 GPa [10]. The discrepancy in these strength values that results from different polishing techniques is significant. It suggests that microfabricated silicon dies with features that penetrate 3µm or more could have severely decreased fracture strength values. This emphasizes the need for a wide scale study to determine the fracture strength of MEMS structures that have been subjected to different fabrication processes.

In addition to investigating polishing effects on fracture strength, Hu tested polysilicon and quartz overlays, as well as argon implantation with and without annealing processes. The results of these tests show that the overlays did not have a significant effect on fracture strength. The difference between argon implanted wafers with and without a subsequent one-step annealing process was significant, with non-annealed wafers showing a fracture strength of 1.6 Gpa and annealed wafers showing a fracture strength of 2.3 Gpa [10]. Hu's work demonstrates the large variability in quasi-static fracture strength of silicon wafers due to different processing techniques and materials used. The variability of fracture strength in MEMS devices is even larger because in addition to the wafer-level processing

techniques described above, MEMS devices undergo further processing to create the structural elements that define their functions.

The structure-level (as opposed to waver level) processing steps typically involve wet or dry etchants that are either anisotropic or isotropic. Yi and Kim performed a number of uniaxial tension tests on beam microscale beam specimens that were created using four etchants: potassium hydroxide (KOH), ethylenediamine-pyrocatechol-water solution (EDP), xenon difluoride (XeF2), and Tetramethylammonium hydroxide (TMAH) [7]. A diagram and an image of one of the microbeam specimens is on the following page.

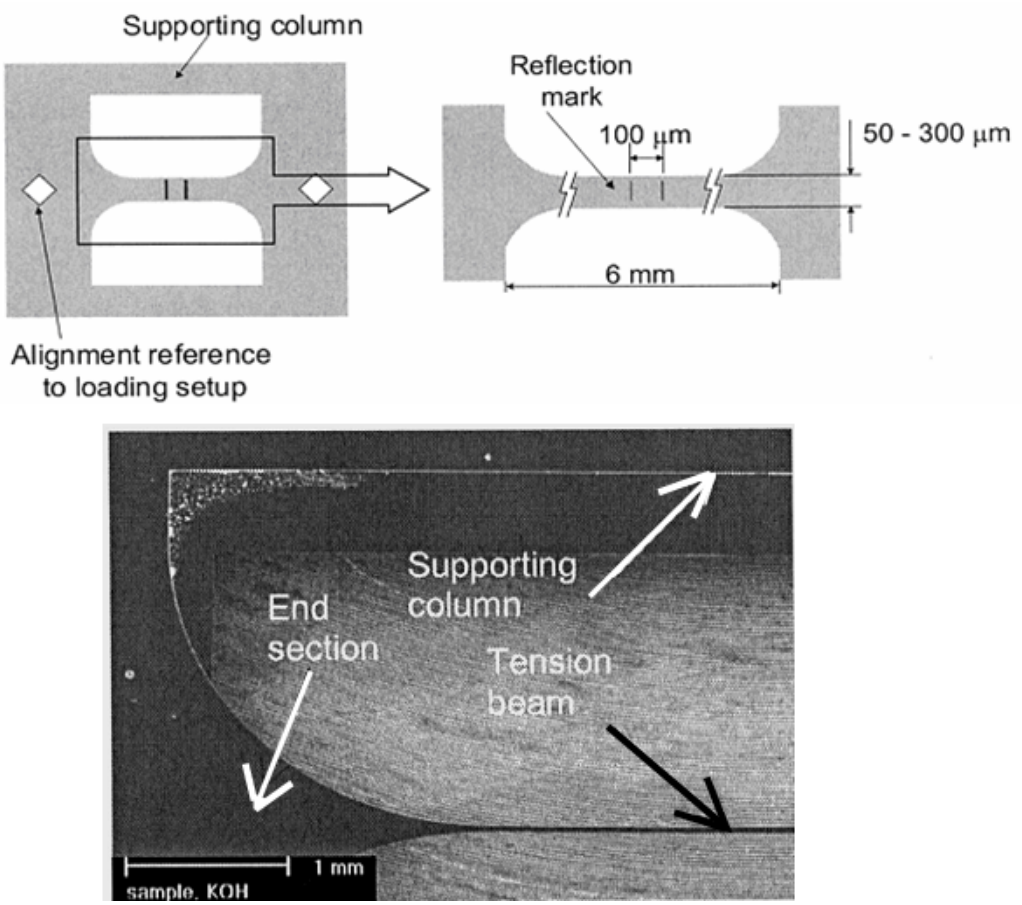

Figure 2. Diagram of a microbeam test specimen (top) and SEM image of one end of a microbeam used for uniaxial tensile testing (bottom) [7]

The uniaxial tension test setup described in the previous section was used to test the microbeams shown above. The fracture strength measurements showed averages ranging from 0.66 GPa for KOH to 1.22 GPa for EDP. In their article, Yi and Kim demonstrate that XeF_2 showed comparable strength values to EDP and TMAH. This result is interesting because the EDP and TMAH etching resulted in the appearance of smooth {111} planes while the isotropic XeF_2 etch resulted in a rougher surface. From the comparable strength values for EDP, TMAH, and XeF_2 despite their surface roughness differences, one would not expect the significant

surface roughness difference between the EDP and KOH samples to result in dramatically different strength values. However, it was demonstrated that the strength of the KOH samples was half that of the EDP samples [7]. From this study, Yi and Kim concluded that in addition to surface roughness, surface morphology must be examined to predict strength values for various etchants.

Like Yi and Kim, Chen et al performed extensive testing on the effect of surface roughness on fracture strength. Using a DEKTAC 3 profilometer, the surface roughness created by various finishes were measured [11]. These finishes, with the roughest listed first and the smoothest listed last, included mechanical grinding, DRIE, wet KOH etch, and chemical polishing. Chen et al's research shows that as surface roughness increases, the planar biaxial flexure specimens' strengths decrease. For example, the mechanically ground sample, with a 3µm roughness, exhibited a strength value of 1.2 GPa while the DRIE etched surface, with a roughness of 0.3µm, exhibited a stress of 4.6 GPa [11]. Chen et al also performed further testing on radiused hub flexure specimens to study the effect of horizontal-vertical transitions and stress concentrations. Results demonstrated that a post-DRIE isotropic etch can be used as a strength recovery step. In Chen et al's tests, DRIE processed sample strength increased from 1.51 GPa to 1.8 GPa with a wet isotropic etch and from 1.51 GPa to 2.7 GPa with a SF_6 dry isotropic etch [11]. The wet isotropic etch used was a solution of 5% HF, 55% HNO_3, and 40% DI water [11]. Through their experiments with surface finishes, Chen et al. established a strong correlation between fracture strength and surface roughness. They also determined that a post-DRIE recovery etch step may be useful for achieving higher strength values.

While Chen et al. studied the effect of stress concentrations using the radial hub flexure specimen described above, Suwito et al. studied stress concentrations by testing structures that had 90° corners at their points of reduction. These 90° corners were created to replicate the sharp angles that result from common anisotropic etching techniques [12]. Suwito et al. created their test specimens using the wet anisotropic etchant KOH, as well as other solutions to remove intermediate processing layers [12]. They found that fractures typically initiated at the 90° sharp corners and that the ultimate tensile strength was 1.21 GPa in the <110> direction of single crystal silicon [12].

From the discussion above, it is clear that an enormous amount of variability exists regarding the quasi-static fracture strength of single crystal silicon in MEMS devices. Polishing techniques, annealing procedures, stress concentration size and location, and the size of the specimen being tested all affect the fracture strength of single crystal silicon. In addition to these considerations, etchant directionality, sample surface morphology and roughness, and post-etch procedures have been shown to have a significant impact on fracture strength. Because of the wide variability in fracture strength data due to the influence of various preprocessing procedures, it is evident that a database of single crystal silicon fracture strength values with corresponding test conditions would be beneficial to MEMS designers.

Dynamic Fracture Strength of Single Crystal Silicon

Although a large amount of research has been performed to determine the fracture strength of single crystal silicon in quasi-static conditions, very little research has focused on determining its dynamic fracture strength. Research on this topic is

important because the quasi-static fracture strength value of single crystal silicon is not necessarily equivalent to that of the dynamic fracture strength. Furthermore, many common MEMS devices such as gyroscopes and accelerometers are operated in dynamic conditions and better knowledge of the mechanical properties of single crystal silicon in dynamic conditions will aid in the virtual qualification process for these structures.

A group at the University of Heidelberg has demonstrated the use of nonlinear surface acoustic wave (SAW) pulses to study dynamic crack nucleation. In their study, Nd: YAG laser ablation was used to excite the nonlinear SAW pulses [13]. Prior to excitation, the bulk silicon surface was covered with an absorbent aqueous suspension layer. When this layer was irradiated, overheating and explosive evaporation occurred, creating a very large transient force on the test structure [13]. They estimated that cracks propagated along the {111} cleavage planes, which is common for single crystal silicon.

In addition to experimentation with bulk, unprocessed single crystal silicon, the Heidelberg group performed numerical analysis to determine the maximum tensile stress of the test structures [13]. They estimated that the stresses for crack nucleation were between 5-7 GPa. These values, however, were found through tensor analysis and only represent predicted values.

Conclusion

The research discussed in this literature review is a sampling of the work that has been performed with single crystal silicon fracture. It is evident that there has been an enormous bias toward quasi-static testing and that minimal attention has been

paid to dynamic loading, or high shock testing. Even the research most relevant to this project, from the group at the University of Heidelberg, lacks a fracture stress measurement method and instead relies upon numerical analysis. Furthermore, their research can only be performed on bulk single crystal silicon that has not been processed and therefore does contain etched features. The research presented in this thesis will provide a straightforward and inexpensive dynamic testing method and post-testing analysis procedures. Furthermore, dynamic fracture strength values for bending of DRIE processed single crystal silicon around the <110> and <100> directions are determined and compared to pertinent fracture strength values from previous work.

Chapter 3: Test Methods

Test Specimens

As discussed in the introduction, prior research on the dynamic fracture strength of single crystal silicon was performed using bulk silicon. The goal of this project is to determine the dynamic fracture strength of single crystal silicon subjected to conditions typically found in electronic devices and MEMS. Therefore, instead of using bulk silicon for this study, specimens with geometries and structures common in MEMS devices were fabricated for testing. It was determined that for this study, simple proof masses on cantilever beams would be used. This basic geometry simplified device fabrication and the analytical maximum stress calculations that will be described subsequently.

The shock test structures were fabricated on silicon-on-insulator (SOI) substrates with handle wafer thicknesses of 425 microns, device layer thicknesses of 100 microns, and buried oxide layer thicknesses of 3 microns. (100) p-type single crystal silicon was used for both the device layer and the handle wafer. These shock test specimens were supplied by QinetiQ. Because the goal of this project is to test MEMS structures that mimic those found in commercial or military devices, the shock test specimens were subjected to very common processing techniques such as photolithography, deep reactive ion etching (DRIE), and an isotropic oxide etch.

The MEMS shock test structures were categorized into two groups: in-plane bending structures and out-of-plane bending structures. There were two separate geometry configurations for the in-plane bending structures and only one for the out-

of-plane structures. A set of parametric structures exists for each of these geometries. The mask layout for each of these parametric structures is shown in Figure 3.

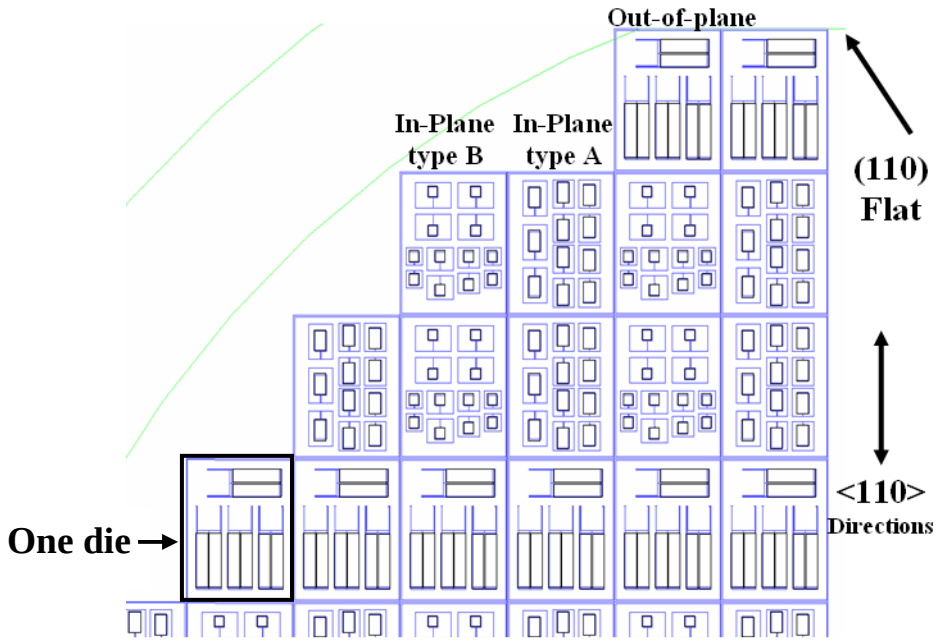

Figure 3. Mask Layout for MEMS Test Specimens

As depicted in the figure above, there are three different test specimen geometries: out-of-plane, in-plane type A, and in-plane type B. The “in-plane” and “out-of-plane” titles represent the critical loading directions of the test structures and will be discussed subsequently. Each large rectangle in Figure 3 represents a die containing a set of test specimens with the same geometry. The out-of-plane structures consist of a proof mass with two cantilever supports. The in-plane structures consist of a proof mass with a single cantilever support. The (110) flat denoted in Figure 3 identifies the crystallographic orientation of the silicon wafer. Using this flat, the <110> family of directions was determined and is also depicted in the figure. Note that all of the

cantilever beams are oriented along the <110> family of directions as well. An alternative representation of the three shock test structures, which clearly depicts their basic shapes, is presented in Figure 4.

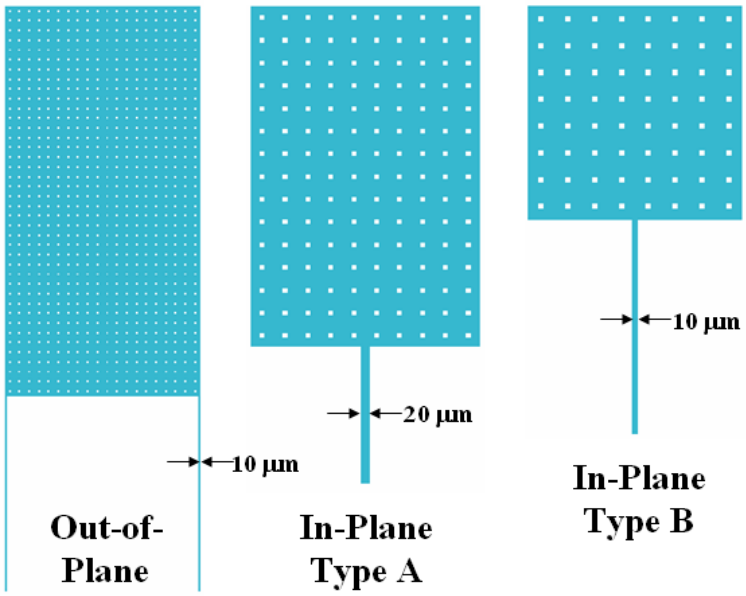

Figure 4. Test Specimen Geometries (Not to scale)

Figure 4 above shows that each of the shock test structures has different proof mass and cantilever beam dimensions. Tiny 10x10 micron square holes are also evident in the proof masses. These holes were incorporated into the structures to allow for easier release of the proof masses from the substrate during the isotropic oxide etch. As previously discussed, each device type contains multiple parametric geometries. The in-plane structure parametric geometries have varying cantilever lengths. These varying cantilever lengths, as well as the proof mass dimensions for each shock test structure specimen, are depicted in Table 1 on the following page.

Table 1. Dimensions of Shock Test Specimens

Device Type	Proof Mass Dimensions		Cantilever Beam Dimensions		Overall Thickness (µm)
	Length (µm)	Width (µm)	Length (µm)	Width (µm)	
Out-of-Plane	2000	1000	1000	10	100
In-Plane Type A	750	500	100, 200, 300	20	100
In-Plane Type B	400	400	100, 200, 300, 400	10	100

Through examination of the number of cantilever beam lengths in Table 1 above, it is evident that there are three in-plane type A parametric geometries and four in-plane type B parametric geometries. For the out-of-plane devices, however, the difference in parametric geometry is based not on cantilever length but instead on gap width. This metric, gap width, is defined as the distance between the cantilevers beams and the side walls. The intention of fabricating structures with various gap widths was to determine if feature size significantly influences the dynamic fracture strength of single crystal silicon. For this study, the out-of-plane device parametric geometries contained gap widths of 5, 10, 15, and 20 microns. The gap widths for the in-plane type A devices were 200 microns for the short (100 and 200 micron) cantilever beams and 250 microns for the long (300 micron) cantilever beams. The gap widths for the in-plane type B devices were 150, 250, 350, and 550 microns for the 100, 200, 300, and 400 micron long cantilever beams, respectively.

Determination of Critical Loading

Initial pre-test calculations were performed to determine the "worst case" loading condition for each device type. These calculations to find the maximum stress for a given acceleration were fairly straightforward due to the simplicity of the shock test structure geometries. To determine the "worst case," or critical loading orientation for each device type, in-plane, out-of-plane, and axial static stress calculations were performed. For these calculations, a 5,000g load was applied. The results are shown below in Table 2.

Table 2. Static stress values for test devices with various loading orientations [14]

Device	Length (μm)	Loading Direction	Static Stress (GPa)	Location
Out-of-Plane	1000	Axial	0.0110	Along Cantilever
		In-Plane	0.1015	Wall Support
		Out-of-Plane	1.3152	Wall Support
In-Plane Type A	100	Axial	0.0021	Along Cantilever
		In-Plane	0.2928	Wall Support
		Out-of-Plane	0.0586	Wall Support
	200	Axial	0.0021	Along Cantilever
		In-Plane	0.3545	Wall Support
		Out-of-Plane	0.0709	Wall Support
	300	Axial	0.0021	Along Cantilever
		In-Plane	0.4162	Wall Support
		Out-of-Plane	0.0832	Wall Support
In-Plane Type B	100	Axial	0.0018	Along Cantilever
		In-Plane	0.3157	Wall Support
		Out-of-Plane	0.0316	Wall Support
	200	Axial	0.0018	Along Cantilever
		In-Plane	0.4209	Wall Support
		Out-of-Plane	0.0421	Wall Support
	300	Axial	0.0018	Along Cantilever

		In-Plane	0.5261	Wall Support
		Out-of-Plane	0.0526	Wall Support
	400	Axial	0.0018	Along Cantilever
		In-Plane	0.6313	Wall Support
		Out-of-Plane	0.0631	Wall Support

The highlighted rows in the table above represent the critical loading orientations for each of the test specimens. The critical loading direction for the out-of-plane devices is out-of-plane whereas the critical loading direction for both the in-plane type A and in-plane type B devices is in-plane. In addition to depicting the critical loading directions, the table above shows that the location of maximum stress is at the wall support, or cantilever base, for each test structure. Furthermore, the table confirms that maximum stress is a function of cantilever length and therefore the longest cantilever structures should fail first.

The stress values in the table above are for static conditions. However, it is assumed that our system is an undamped, single degree-of-freedom system subjected to a step acceleration pulse. This assumption allows for an amplification factor of 2 to be used to determine a maximum dynamic stress value estimate [15]. This procedure was used to predict maximum dynamic stress values for the MEMS shock test structures subjected to 3,000g and 5,000g acceleration pulses before testing.

Sample Preparation

Prior to testing, a number of sample preparation steps were performed. In order to carry out accurate post-testing analysis of the MEMS structures, pre-testing visualization was required. This visualization step involved the use of an

environmental scanning electron microscope (ESEM). This step was performed to determine if any of the samples contained broken or immobile proof masses or were covered with debris. If any of the samples were found to be defective for the reasons above, they were eliminated from the sample population and were not included in the post-testing procedures. A pre-testing ESEM image depicting some non-functional test devices is shown below:

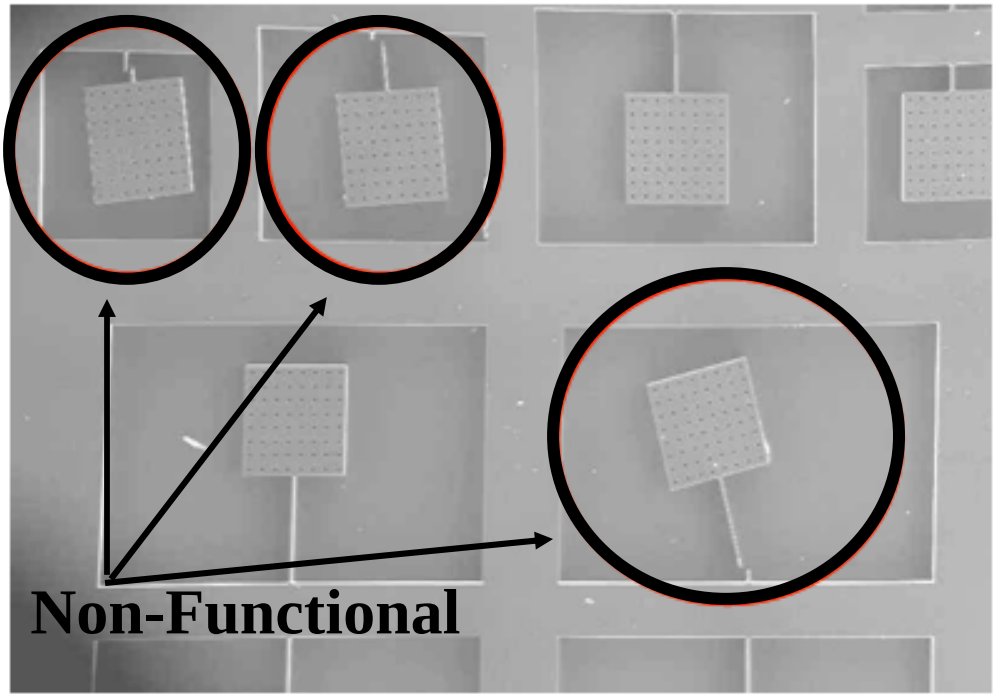

Figure 5. ESEM image of an In-Plane Type-B die with non-functional devices circled

In cases where many test structures on a die were broken prior to drop testing, another die with intact structures was be chosen instead. If a die with 100% intact structures was not available, the devices with broken structures were noted and these devices were not included in post-testing analysis. This process ensured that the presence of

damaged samples prior to testing did not influence the shock testing results by artificially increasing the number of failed samples.

After examining each shock test structure, the die were attached to fixtures that were then mounted to the drop tower table. Each fixture consisted of an aluminum block with a bolt hole that allowed for coupling to the drop tower. The dimensions of these fixtures were 32 × 32 × 15 mm. A picture of a fixture is shown in Figure 6 below.

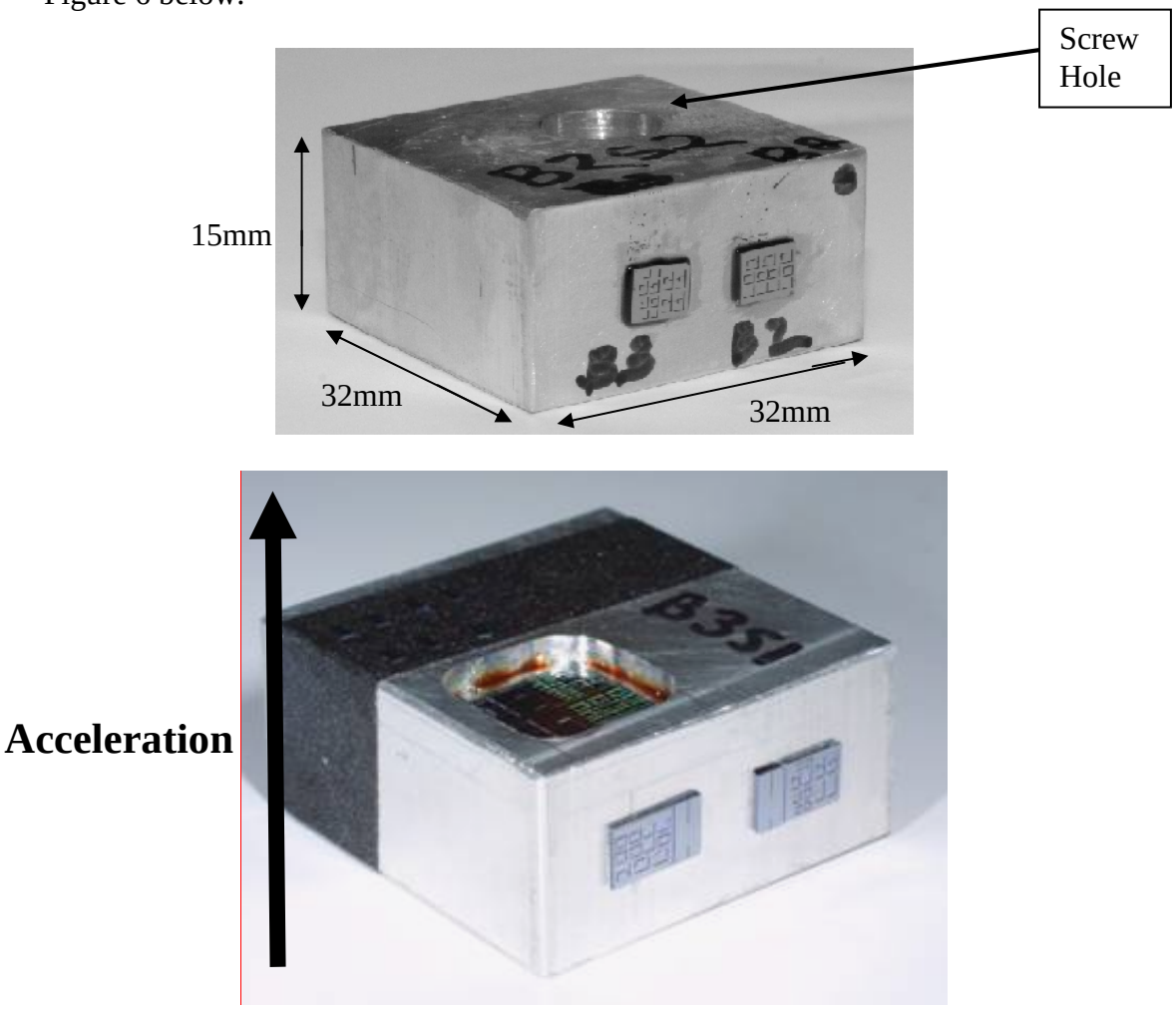

Figure 6. Two test fixtures showing dimensions and screw hole (top) and direction of acceleration (bottom). The in-plane devices are on the side of the test fixture whereas the out-of-plane devices are in the test fixture pocket (bottom).

When out-of-plane structures were being tested, a pocket in the aluminum block was also created and the die were placed in that pocket. This allowed the proof masses on the out-of-plane structures to move freely without incurring damage from hitting the drop tower table upon impact. A diagram of a test fixture showing this arrangement is below.

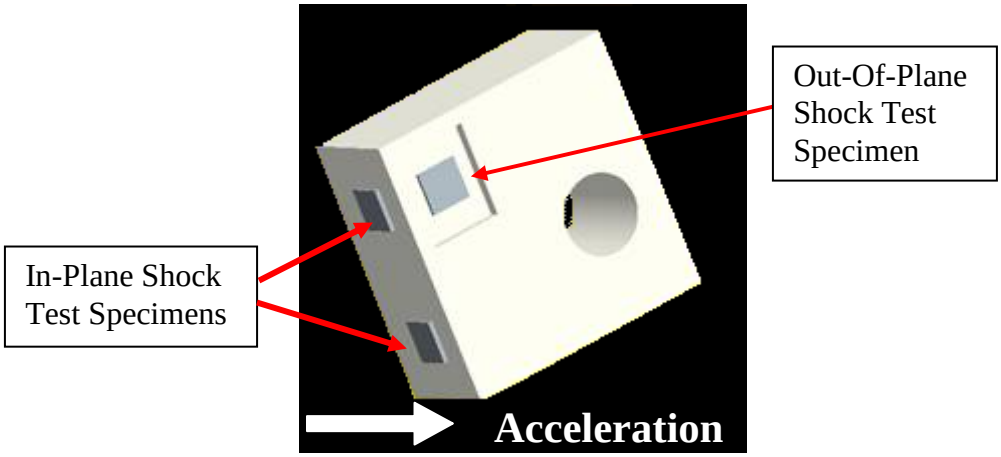

Figure 7. Diagram of an aluminum test fixture with MEMS die attached

EPO-TEK ® 353ND adhesive was used to attach the die to the aluminum fixtures. This epoxy was selected to ensure that the bond would survive loads greater than 5,000g [16]. To cure the epoxy after application, the aluminum fixtures were placed in a 150°C oven for one hour. After curing, the test specimens were checked again to ensure that all structures were intact. If damaged structures were identified, these would be noted and eliminated from post-testing analysis.

Test Setup

Drop testing was chosen as the method to subject the MEMS specimens to various dynamic stress levels for a variety of reasons. Drop testing is a very popular method for dynamic testing because it provides a high acceleration environment up to 5,000g, it is inexpensive compared to other methods such as air gun testing, and it provides reproducible results. In addition to these benefits, shock amplitude and shock duration can be adjusted by placing various materials of different thicknesses between the drop table and the base.

For this research, both a Lansmont 23-D shock tester and an MTS IMPAC66 vertical shock machine were used. Each of these shock towers is able to produce half-sine pulses with shock durations of fractions of a millisecond. However, the MTS IMPAC66 shock tower is capable of achieving higher accelerations than the smaller Lansmont 23-D shock tower. Half-sine pulses of typical 3,000g and 5,000g acceleration profiles for these two machines are below in Figure 8. The MTS IMPAC66 vertical shock machine was used to achieve the 5,000g acceleration pulse while the Lansmont 23-D shock tester was used for the 3,000g acceleration pulse.

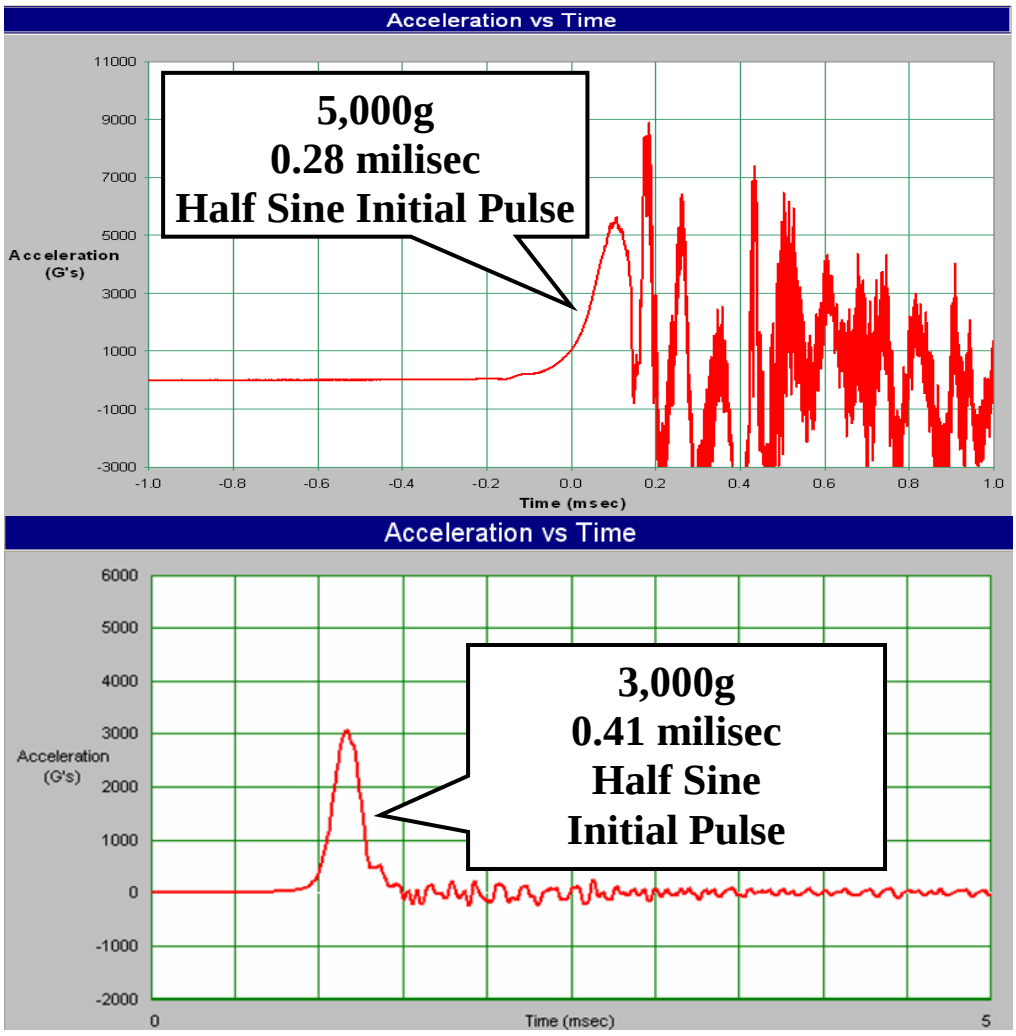

Figure 8. Typical Half-Sine Pulses for a 3,000g and a 5,000g acceleration profile

Through examination of these pulses of different magnitudes, it is evident that lower accelerations result in both cleaner pulses and longer pulse durations. Although this is the general trend, it is important to note that fluctuations in environmental conditions, such as humidity, as well as changes in the material between the drop table and the base, do cause variations in drop tower performance. For example, a test from a 26" (650mm) drop table height resulted in a maximum acceleration of 1975g during one set of experiments. However, the same test was performed one month later

and the result was a maximum acceleration of 1651g. This discrepancy in acceleration magnitude stems from environmental fluctuations and physical changes in the material between the drop tower table and base over time.

To account for the fluctuations described above, a series of calibration drop tests were performed prior to each MEMS shock structure test. The calibration procedures involved five to eight drops tests over a range of table heights with no test specimens attached. Once these tests were performed, a plot of drop height vs. acceleration was created. Using this plot, drop heights that corresponded to specific accelerations could be extrapolated.

An accelerometer was directly attached to the drop tower table to monitor acceleration throughout the test. The accelerometer used for the Lansmont 23-D tower was a model 350B23-ICP® from PCB Piezotronics. This specific model was chosen for its 10,000g measurement maximum and for its high sensitivity of 0.372mV/g at 100 Hz. The accelerometer used for the MTS IMAC66 vertical shock machine tests were Endevco 7270A-20KM6 and Endevco 2255B-01 models.

A variety of methods used to mount the accelerometer to the drop tower table were considered. Temporary adhesive mounts such as hot glue or wax are often used to secure the accelerometer to the table for temporary and limited use. A disadvantage of these mounts is that they sometimes result in a reduction in high-frequency range [17]. Furthermore, the success of adhesive mounts is tied strongly to the volume of adhesive used and the proper selection of a smooth attachment surface. As a result, continuity between tests can be difficult to achieve when using adhesive mounts. Because of the large quantity of tests being performed and the need for an

accelerometer installation method which allows for easy attachment and removal from the drop tower table, a temporary adhesive mount was not chosen. An alternative to temporary adhesive mounts are permanent, direct adhesive mounts. Unfortunately, because many different laboratory researchers use the drop tower at the University of Maryland CALCE facility, permanent attachment of the accelerometer was not a feasible option either. Instead, a mechanical attachment solution was chosen because it allowed for simple installation and removal of the accelerometer without compromising the monitoring performance of the device.

The fixture used to mount the accelerometer to the drop tower table was an aluminum block that contained two holes. The larger, unthreaded bolt hole was used to secure the aluminum block to the drop tower table and the smaller, threaded hole was for the coupling of the accelerometer to the aluminum block. An image of this fixture is shown below.

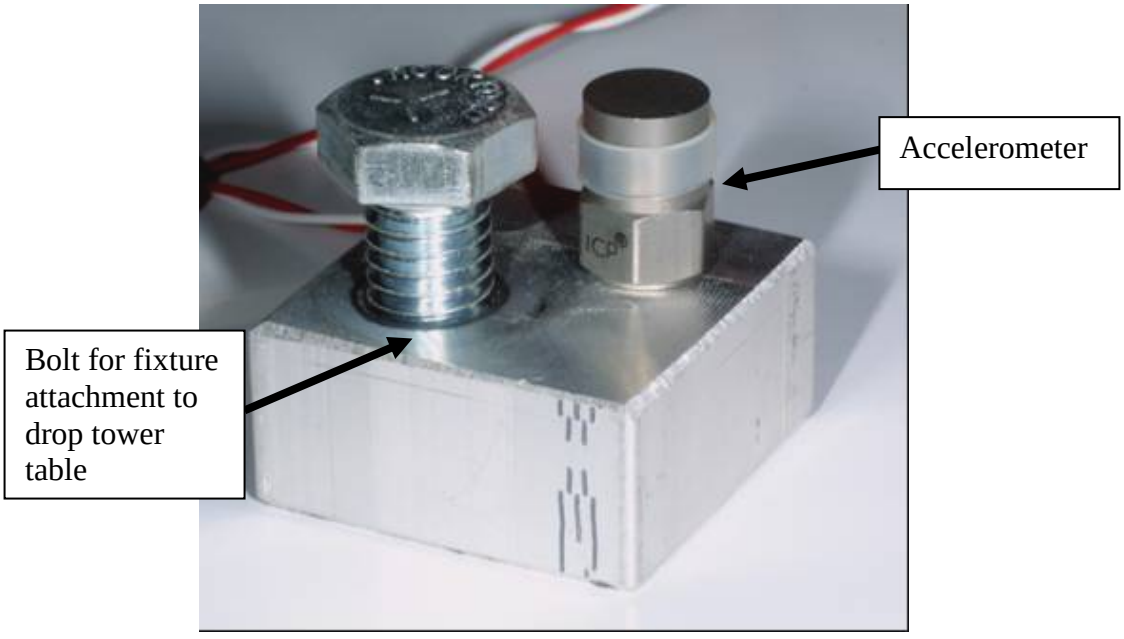

Figure 9. Fixture used to attach the accelerometer to the drop tower table

To accurately monitor the acceleration experienced by the MEMS devices throughout the drop test, the accelerometer fixture was mounted in close proximity to the test devices on the drop tower table. The image below shows the setup of the accelerometer and the MEMS test specimens on the drop tower table.

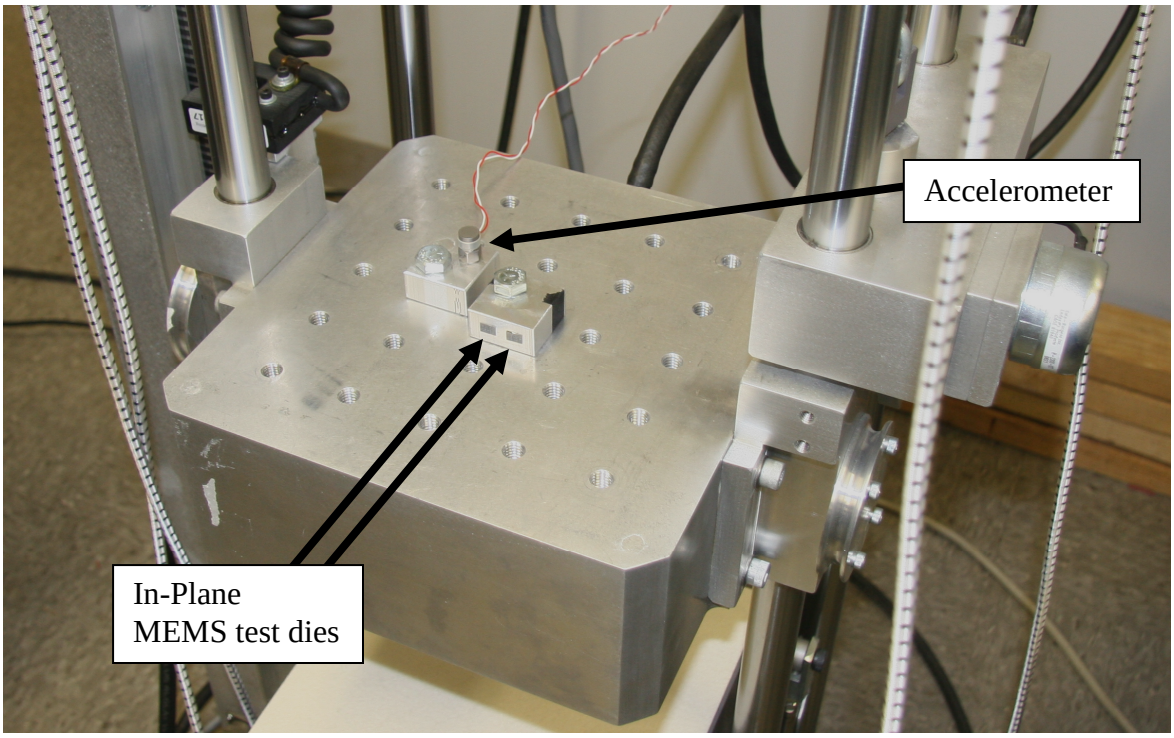

Figure 10. Drop Tower Setup

In order to log the acceleration data generated by the accelerometers, the Test Partner 3 (TP3) program provided by Lansmont was used. This program allowed for data acquisition as well as visualization of the acceleration profiles. Prior to testing, TP3 allows the user to specify a desired recording time, trigger level, and trigger polarity. The program also requires information about the accelerometer, including its sensitivity and full scale measurement capability. To test the MEMS shock structures, a recording time of 2ms and a sampling rate of 500,000 samples per second were used. This recording time interval was selected to provide the highest

sampling rate possible while still capturing the entire pulse duration or pulse width. To prevent premature sampling, the TP3 program requires a trigger input as a percentage of the accelerometer's full scale recording ability. A percentage of 6% was specified for testing. This percentage value was sufficient to ensure that data acquisition did not begin until the drop test had begun.

In addition to setting a 6% trigger, a number of other steps were performed to ensure that the recorded data truly represented the drop test acceleration profile experienced by the MEMS devices. One of these steps was taping down the wire that led from the accelerometer to the data acquisition unit. This wire was taped along the rear hose of the drop tower. Immobilizing the extra wire length prevented the wire from whipping around during the test and thus prevented any electrical signal degradation or interruption from occurring as a result. The second step taken to ensure correct data collection involved modifying the standard sequence of actions used to actuate the drop tower. Typically, the data acquisition software can be placed in "record data" mode prior to dropping the table. However, the acts of raising the table to the desired height and actuating the drop from that desired height caused acceleration spikes which surpassed the trigger acceleration level. Even raising the trigger level to over 25% did not mitigate this premature triggering problem. Therefore, instead of turning the software to "record data" mode prior to moving the drop tower table, the table was raised to the desired drop height first. After reaching this height, the drop tower was actuated at the same instant that software was set in "record data" mode. This process, although somewhat tedious, ensured accurate capturing of the full drop test acceleration profile.

Maximum Dynamic Stress Calculations

To determine the maximum dynamic stress levels to which the MEMS shock test structures were subjected, analytical static stress calculations were performed. These calculations, performed only for critical loading conditions, took into account the measured maximum accelerations and pulse durations of the drop tests. Examples of an out-of-plane bending calculation and an in-plane bending calculation are described below.

To evaluate the out-of-plane test structures, a free body diagram was created. This is shown below in Figure 11.

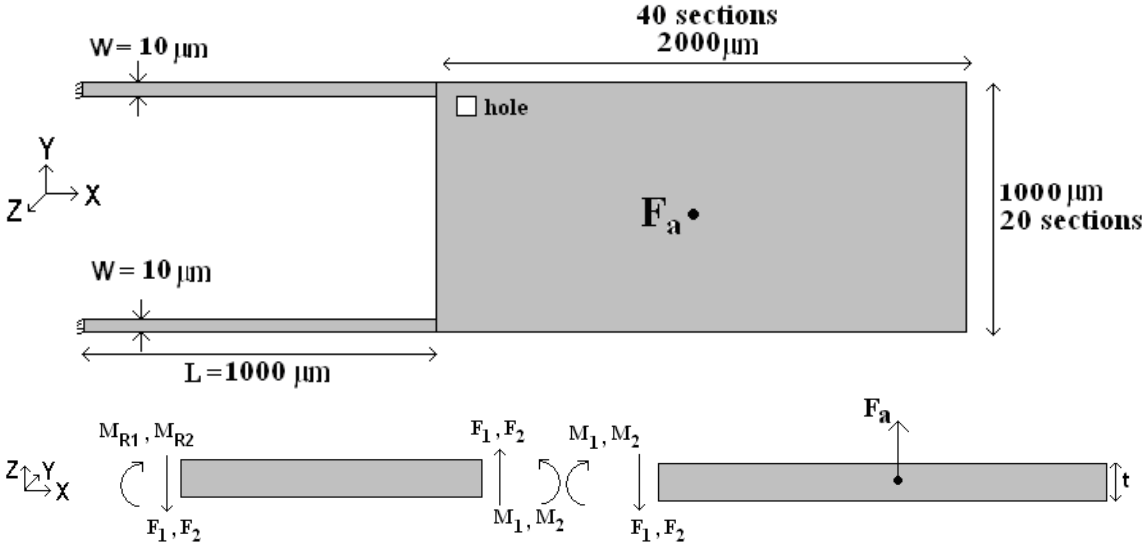

Figure 11. An out-of-plane test structure and its free body diagram (out-of-plane bending)

First, the section mass, M_s, was determined. As described previously, a number of 10x10 micron holes are spaced equally apart on the proof mass. To determine the total mass of the proof mass, it was divided into 50x50 micron sections, with each

section containing one 10x10 micron hole. This section mass was then equivalent across all in-plane and out-of-plane test structures and was calculated through equation 1.1.

$$M_s = [\text{section area - hole area}](\rho)(t) \tag{1.1}$$

In equation 1.1, *t* is the thickness of the device layer while ρ represents the density of single crystal silicon. To find the applied force, F_a, due to a 5,000g acceleration, a simple application of Newton's second law was performed. This is shown in equation 1.2 below.

$$F_a = ma = [M_s((20*40)\text{sections})]\left[5{,}000g * 9.8\frac{\text{m}}{\text{sec}^2}\right] \tag{1.2}$$

Next, the forces, F_1 and F_2, and the moments, M_1 and M_2, were calculated. These calculations were simplified due to symmetry in both geometry and loading.

$$F_1 = F_2 = F_a/2 \tag{1.3}$$

$$M_1 = M_2 = (F_a/2)*(L_{PM}/2) \tag{1.4}$$

In equation 1.4 above, L_{PM} is the total length of the proof mass, 2000 microns. Once the moments at the base of the proof mass were calculated, the reaction moments M_{R1} and M_{R2} were found using equation 1.5.

$$M_{R1} = M_{R2} = F_2 * L + M_2 \tag{1.5}$$

To solve for the maximum static stress, σ_x, the moment of inertia, I_y, is required because the proof mass rotates about the y-axis. I_y is found through equation 1.6

$$I_Y = \frac{1}{12}t^3 w \tag{1.6}$$

In equation 1.6, *t* is the thickness of the device layer and *w* is the width of the cantilever beam. Finally, the maximum static stress at the wall support can be found using the reaction moments and the moment of inertia. This is shown in equation 1.7.

$$\sigma_x = \frac{M_{R2}(t/2)}{I_Y} \tag{1.7}$$

For the 5,000g assumed acceleration, the maximum static stress was found to be 1.32 GPa. To streamline the calculation process, a MATLAB program was written to find σ_x using the procedure described above. This file is located in appendix A.

For the in-plane MEMS test structures, a very similar process was used to find the maximum static stresses. The only changes in the process stem from the difference in geometries, the existence of a single cantilever beam on the in-plane devices, and the discrepancy in critical loading directions of the in-plane and out-of-plane devices. Although the analytical process steps remain similar, the variation of in-plane structure cantilever lengths does require additional calculations. For example, the maximum static stress for all of the out-of-plane devices at a given acceleration is the same. However, at a given acceleration, the maximum static stress for the in-plane devices is not identical and varies with cantilever length. In-plane type-A and type-B device calculations confirm the intuitive principle that the maximum static stress increases as cantilever length increases. This trend is demonstrated below in Table 3 below.

Table 3. Static stress values for in-plane devices with 5000g assumed acceleration

In-Plane Type A Devices	
Cantilever Length (μm)	**σ_x (GPa)**
100	0.2928
200	0.3545
300	0.4162
In-Plane Type B Devices	
Cantilever Length (μm)	**σ_x (GPa)**
100	0.3157
200	0.4209
300	0.5261
400	0.6313

As with the out-of-plane devices, the analytic calculation steps and MATLAB codes for in-plane Type A and in-plane Type B devices are located in appendix A.

After the maximum static stress value for a given acceleration was found through the analytic calculations described above, the dynamic stress was found using the Sloan equations [18]. Instead of assuming the dynamic stress to be double that of the static stress, the Sloan equations employ a shock amplification value. The equations approximate the actual single degree of freedom (SDOF), half sine wave input shock spectrum, which is shown below in Figure 12.

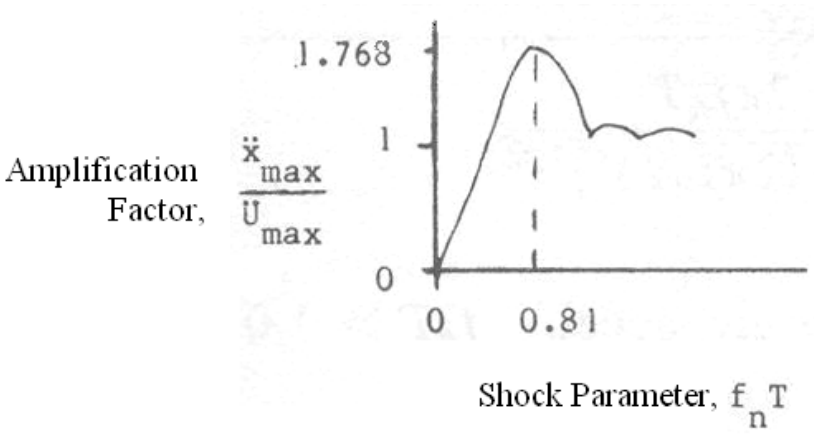

Figure 12. Graph displaying the shock spectrum, which provides amplification factors for given shock parameters [18].

Although the Sloan equations take into account multiple variables to provide a more accurate multiplication factor to find dynamic stress, they can only be used for single degree of freedom, half sine input systems. It is believed, however, that the shock test system utilized meets these requirements. To confirm this belief, these assumptions were tested using a dynamic FEA analysis that is described in detail later in this report.

A shock amplification factor was determined for each drop test because the calculation requires inputs that vary with each test, such as pulse duration and maximum acceleration. In addition to these variables, the natural frequency of the MEMS test structures must be known to determine a shock amplification factor. To find the natural frequency of the test structures, an ANSYS modal analysis was performed. The modal analysis results were also used to determine the effect of the notching found in the shock response in Figure 12. This study can be found in appendix B. Due to the presence of holes in the proof masses, a procedure was

performed to determine whether these holes significantly affected the natural frequencies. This procedure involved carrying out modal analysis on the out-of-plane test structure using both the standard density value of 2330kg/m^3 and a modified density value of 2236kg/m^3, which takes into account the 10x10 micron proof mass holes. This exercise was also performed on an in-plane type B structure with a 400µm long cantilever. Table 4 and Table 5 below show the results of this procedure.

Table 4. Comparison of modal frequencies on out-of-plane structure

Set	**Frequency (assuming density of 2330 kg/m^3)**	**Frequency (assuming density of 2236 kg/m^3)**	**Error %**
1	1434.7	1464.5	2.1
2	2380.6	2340.1	1.7
3	21082	21521	2.1
4	33654	34355	2.1

Table 5. Comparison of modal frequencies on in-plane type B structure

Set	**Frequency (assuming density of 2330 kg/m3)**	**Frequency (assuming density of 2237 kg/m3)**	**Error %**
1	3646.3	3721.3	2.0
2	17212	17566	2.0
3	35490	36220	2.0
4	37370	38139	2.0

As indicated in Table 4 and Table 5, the percent error that results from not taking into account the proof mass holes is very small. Therefore, for subsequent out-

of-plane and in-plane test structure modal analysis procedures, the holes were not modeled and the standard density value of 2330kg/m^3 was used.

The in-plane shock test devices all have different natural frequencies in the in-plane bending direction due to the variation in cantilever length. The out-of-plane shock test devices, however, contain the same proof mass and cantilever geometry and thus have a common natural frequency for out-of-plane motion. Examples of modal solutions for the out-of-plane devices and for an in-plane device are presented in Figure 13 and Figure 14.

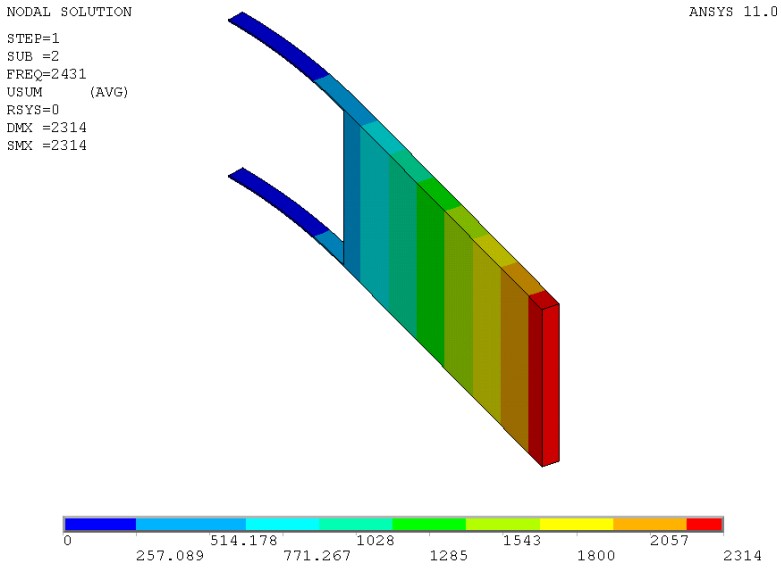

Figure 13. Modal solution for out-of-plane test device

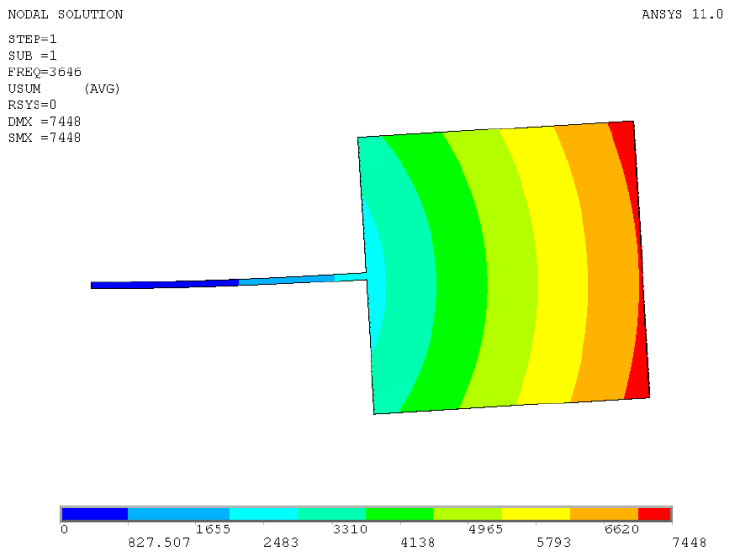

Figure 14. Modal solution for in-plane type B test device (400µm cantilever)

Similar modal analyses were performed for the rest of the MEMS shock test structures. Because the modal analyses return natural frequencies for a number of mode shapes, the correct natural frequency values had to be selected. These correct values correspond to mode shapes that represent the movement of the test devices when subjected to loading in their critical loading direction. The results of this evaluation are tabulated below.

Table 6. Device natural frequency summary

Device	**Cantilever Length (µm)**	**f_n (Hz)**
Out-Of-Plane	1000	2,378
In-Plane Type A	100	11,318
	200	7,406
	300	5,578

In-Plane Type B	100	10,387
	200	6,369
	300	4,550
	400	3,486

Once the fundamental frequency of the test devices was known, the maximum acceleration and pulse duration were gathered from the post-test report in the TP3 program. The Sloan equations, shown below, were then be used to determine appropriate amplification factors [18].

$$Amplification\ Factor = \frac{4 f_n T}{1-4(f_n T)^2}\cos(\pi f_n T), \quad f_n T < 0.5 \qquad (1.8)$$

$$Amplification\ Factor = \frac{2 f_n T}{2 f_n T - 1}\sin(\frac{2\pi}{2 f_n T + 1}), \quad 0.5 < f_n T < 1.5 \qquad (1.9)$$

$$Amplification\ Factor = \frac{2 f_n T}{2 f_n T - 1}\sin(\frac{4\pi}{2 f_n T + 1}), \quad 1.5 < f_n T < 2.5 \qquad (1.10)$$

$$Amplification\ Factor\ ;\ 1, \quad f_n * T > 2.5 \qquad (1.11)$$

A graph depicting the amplification factors listed in equations 1.8 through 1.11 is below in Figure 15. Note that equation 1.10 does not fit the same, continuous curve exhibited by the other equations. This indicates that there is an error in the Sloan equation reference. To correct this error, equation 1.9 is extended over the entire domain 0.5< fnT <2.5.

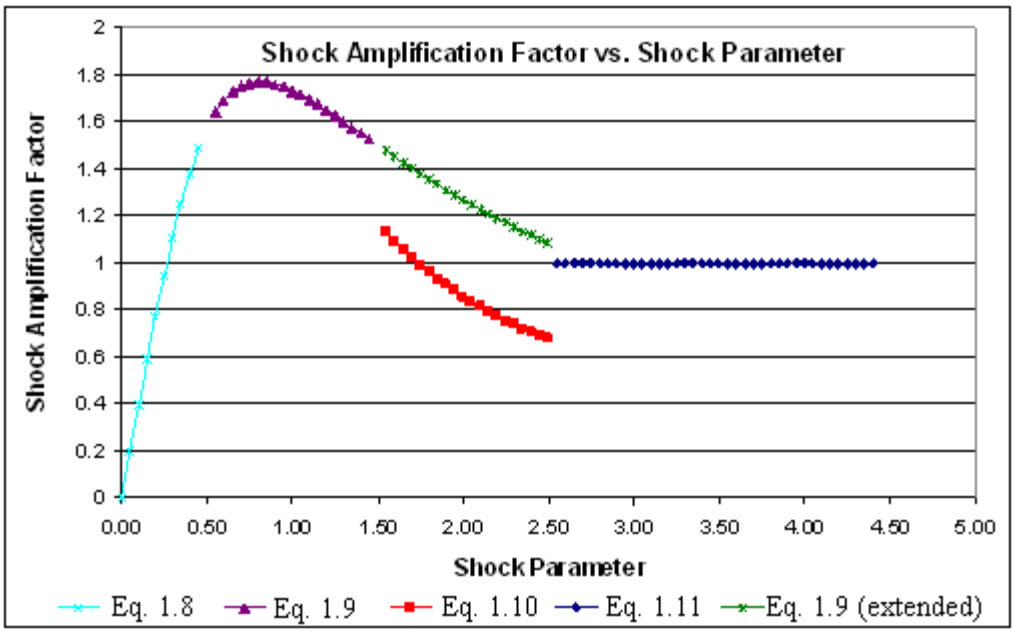

Figure 15. Graph displaying the Sloan equations [14]

Through examination and comparison of Figure 12 and Figure 15, it is evident that the Sloan equations do approximate the actual single degree of freedom, sine wave input shock spectrum. However, to verify the aforementioned assumptions required for use of the Sloan equations, a detailed dynamic FEA analysis was also performed.

Dynamic FEA Analysis

The dynamic FEA analysis performed on Abaqus involved models of an out-of-plane structure and an in-plane type-B device. The type-B devices were chosen for this study because they experience more stress than the type-A devices when subjected to a given acceleration. To increase confidence in the results of this study at various acceleration levels, FEA analysis and SDOF theory calculations were performed for both 3000g and 5000g pulses. For the SDOF calculations, pulse

durations were assumed to be 0.41ms for the 3000g pulse and 0.28ms for the 5000g pulse. Table 7 contains data collected from each of the analyses performed.

Table 7. Chart comparing Sloan equation analytic results (SDOF Theory) with dynamic FEA results [19]

Device	**Length (µm)**	**3000g**		**5000g**	
		Amp. Factor		**Amp. Factor**	
		SDOF Theory	**FEA Analysis**	**SDOF Theory**	**FEA Analysis**
Out-of-Plane	1000	1.74	1.63	1.74	1.59
In-Plane Type B	100	1	1.06	1	1.11
	200	1	1.07	1.35	1.27
	300	1.31	1.26	1.6	1.5
	400	1.53	1.46	1.74	1.63

Examination of Table 7 reveals that the SDOF theory results and those from the FEA analysis are extremely comparable. This correlation is more evident in Figure 16, which is a graphical representation of the data above.

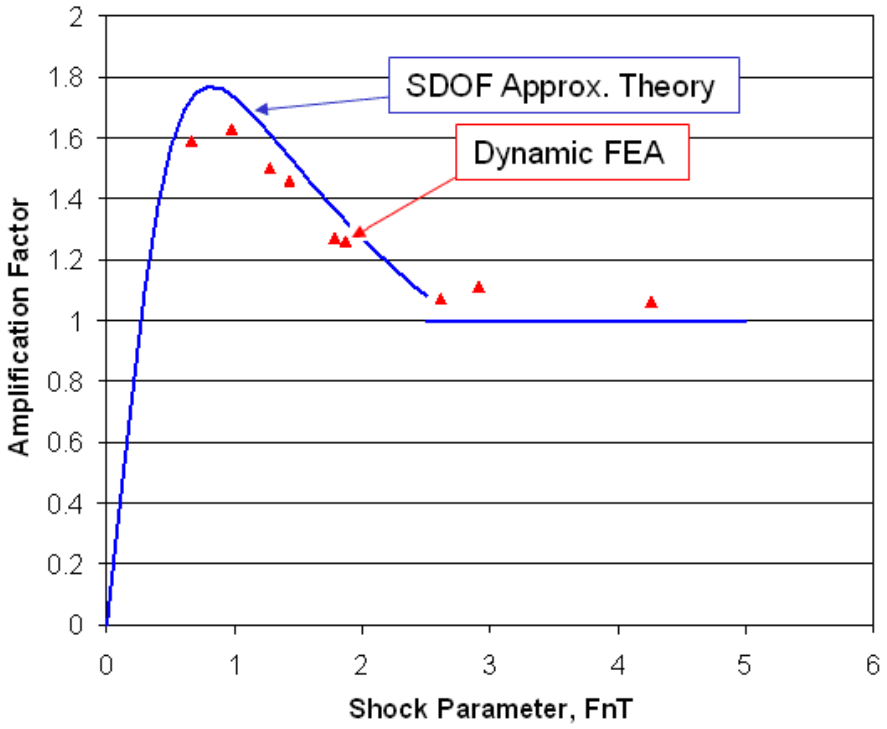

Figure 16. Comparison of Sloan equation analytic results and dynamic FEA results

The SDOF approximation theory values and the dynamic FEA values were within 10% of each other for each device and acceleration level examined. Therefore, it was concluded that the SDOF approximation theory, represented by the Sloan equations, was an accurate and acceptable method to compute dynamic stress values for the shock testing performed in this research. Consequently, the Sloan equations were used to determine all subsequent dynamic stress levels.

Visualization of Samples After Testing

In addition to the post-testing quantitative analysis described above, visualization of the MEMS shocks structures after testing was also performed.

Examination of the broken proof masses and the broken cantilever beams was performed to gain perspective on both failure location and failure mode. However, during testing, the proof masses from the failed structures were dislodged from the single crystal silicon substrate and fell onto the drop tower table. Throughout this fall, the orientation of the proof masses sometimes changed. Figure 17 on the following page shows the behavior of an out-of-plane MEMS shock structure throughout the drop test process.

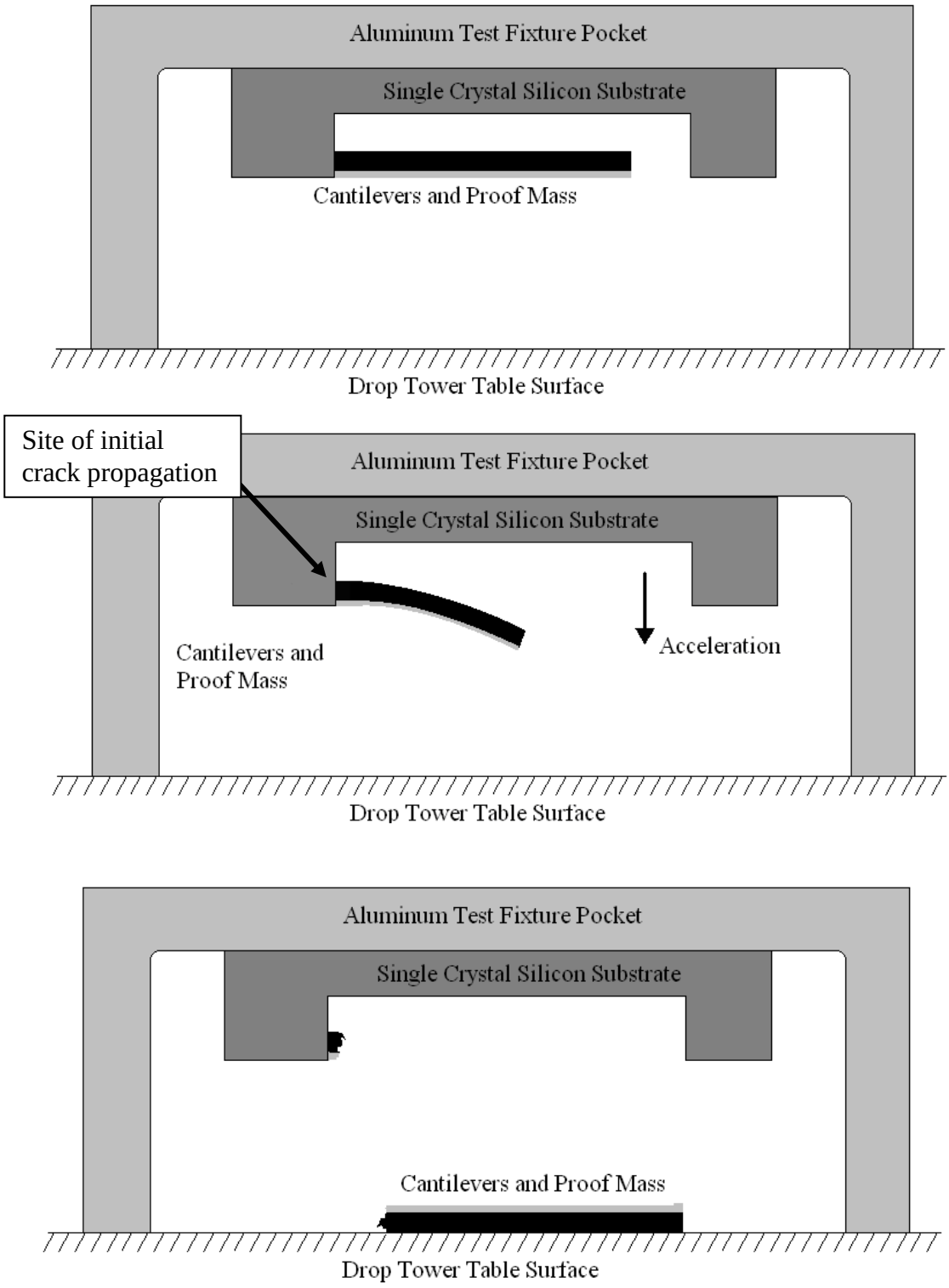

Figure 17. Diagram of MEMS device prior to drop test (top), during a drop test (middle), and after the drop test (bottom)

If the test device failed, the cantilever and proof mass unit fell and eventually landed on the drop tower table surface, as shown on the bottom diagram in Figure 17. To visualize the site of initial crack propagation using environmental scanning electron microcope (ESEM), however, the cantilever and proof mass unit needed to be correctly oriented so that the underside of the deice faced upwards. Unfortunately, the cantilever and proof mass units fell to the drop tower table surface randomly and landed in unpredictable orientations. Therefore, after the test, these units were collected with special rubber-tipped tweezers to prevent handling damage. They were then examined under a light microscope and placed in the required orientation for ESEM.

In Figure 17 above, the top and bottom faces of the proof mass are denoted by the gray and black lines. In reality, however, the two faces of the proof masses were distinguishable through markings surrounding their etch holes, as shown below in Figure 18.

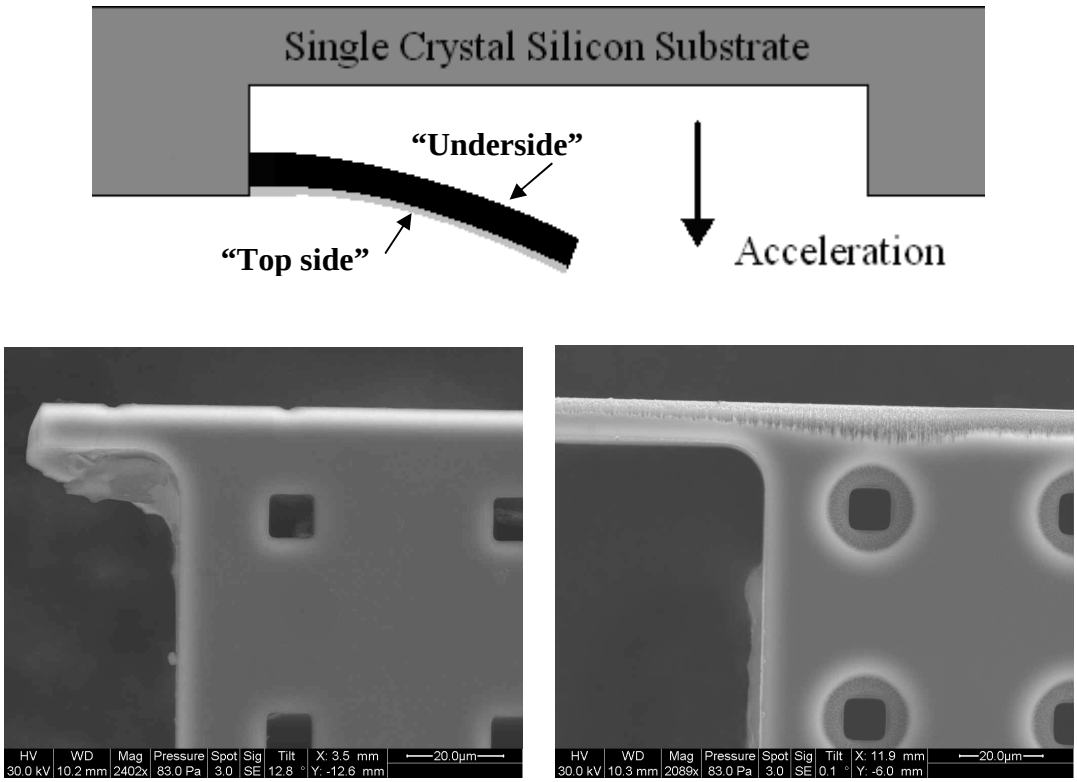

Figure 18. ESEM images of etch holes on the top side of a proof mass (left) and on the underside of a proof mass (right)

The underside of the proof mass, which contains the site of initial crack propagation, is marked by etch holes with circular structures surrounding them. These circles were created by the isotropic oxide etch that was used to release the proof masses from the single crystal silicon substrate. The marks that distinguished each side of the proof mass were instrumental in correctly identifying the required orientation for ESEM. After collecting the detached proof masses from the drop tower table surface, they were examined with an optical microscope, correctly positioned, and then fixed securely onto the aluminum test fixture with double sided tape. An image of the fixture with aligned proof masses is below in Figure 19.

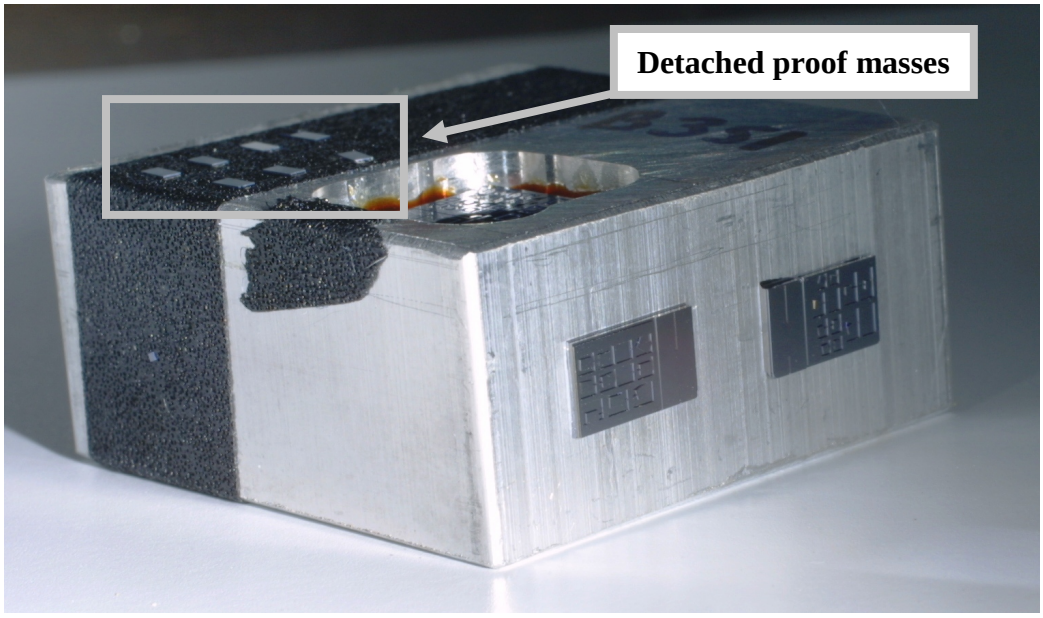

Figure 19. Post-testing aluminum fixture setup for ESEM

Once the proof masses were recovered and secured on the test fixture, the structures were visualized using ESEM. Figure 20 below shows one of the recovered proof masses. Note that the fracture occurred at the base of the cantilever beams, the locations of critical stress.

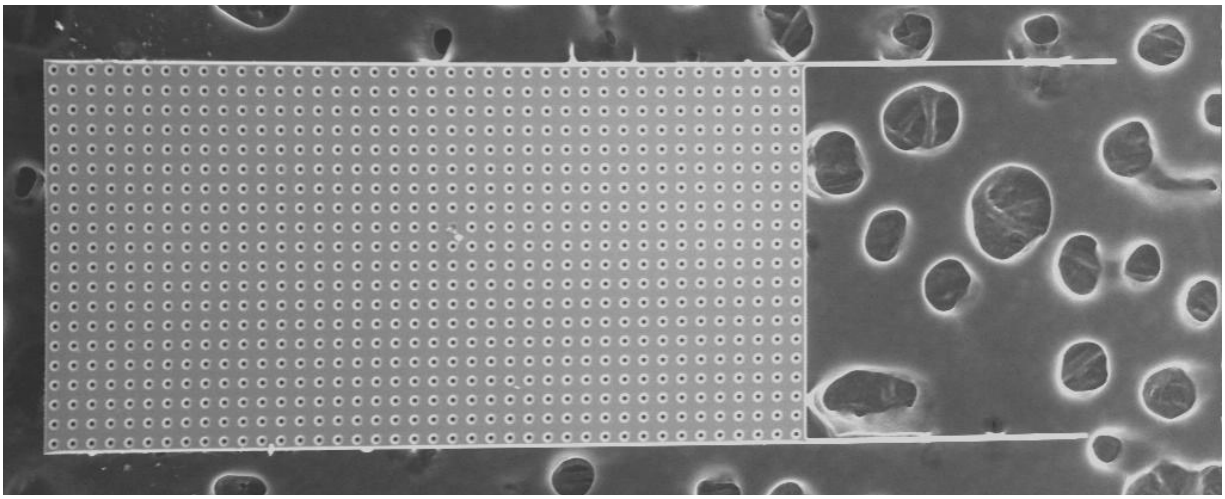

Figure 20. ESEM image of a recovered proof mass on double sided tape

Chapter 4: Results

Introduction

Samples from each group of MEMS shock test structures were initially subjected to a 5,000g acceleration load with the IMPAC 66 shock machine. The result of these tests confirmed the need for lower acceleration load testing for the out-of-plane devices. Therefore, a sequence of lower acceleration tests was performed on these devices. The 5,000g pulse resulted in unpredicted failures for both types of in-plane devices. These results will be discussed in the following section.

In-Plane Test Structures

Both types of in-plane test structures were expected to fail near the base of the cantilever, the location of highest stress. For any given acceleration level, the structures with the longest cantilever beams experience the highest stress. This relationship is demonstrated in Table 3. Therefore, the longest cantilever structures were expected to fail first. For the in-plane type A devices, these are the structures with 300µm cantilevers. For the in-plane type B devices, these are the structures with 400µm cantilevers. However, when the in-plane devices were subjected to 5000g acceleration pulses along their critical loading directions, the shortest cantilever beams within each block type failed instead. Figure 21 shows both types of in-plane structure die in which all of the 100 micron long cantilever beams failed.

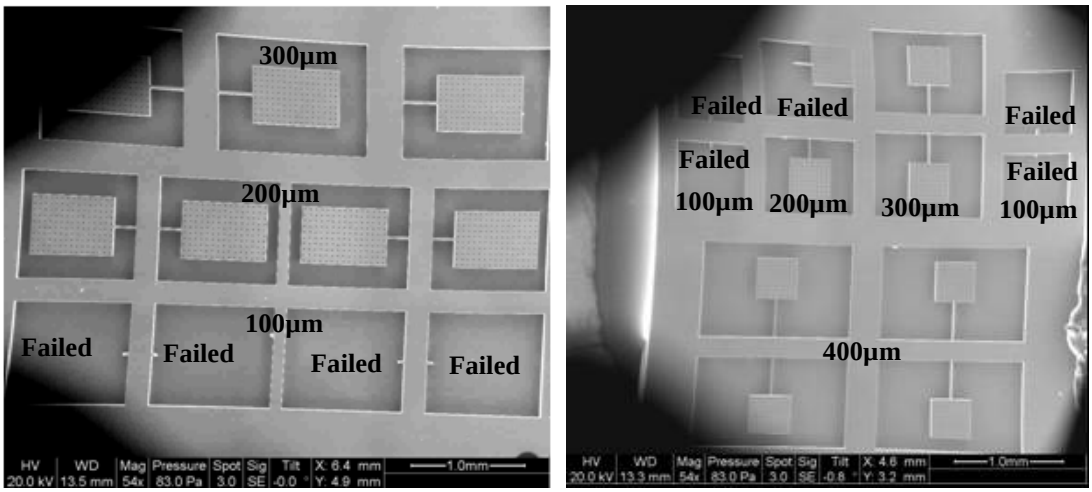

Figure 21. ESEM images of an in-plane type A die (left) and an in-plane type B die (right) that were subjected to a 5000g acceleration pulse

In addition to showing that the 100 micron long cantilever devices failed, Figure 21 also indicates that one of the 200 micron long cantilever beams in the in-plane type B die failed. These results were unpredicted because Table 3 indicates that for a given acceleration, the 100 micron type-B devices experience significantly less stress compared to the other in-plane devices.

Table 8 is a summary of the drop tests performed with the in-plane shock test devices. It shows the failure percentages of these structures when they were subjected to a 5000g acceleration pulse with the larger drop table, the IMPAC66 shock test machine.

Table 8. Failure summary of in-plane shock test structures after 5000g drop tests [14]

Type	Length (µm)	# Tested	% Failure
A	100	20	70.0%
	200	20	0.0%
	300	12	0.0%
B	100	10	100.0%
	200	5	20.0%
	300	6	33.3%
	400	9	0.0%

The table above demonstrates that for both types of in-plane dies, most of the failures occurred in the shorter beams and that no failures were observed among the longest cantilevers. Additional testing was performed to determine whether any of these structures would fail at lower stresses. The in-plane devices were subjected to a 3068g acceleration pulse along their critical loading direction using the Lansmont drop table. Post-test ESEM images of the structures are shown below in Figure 22.

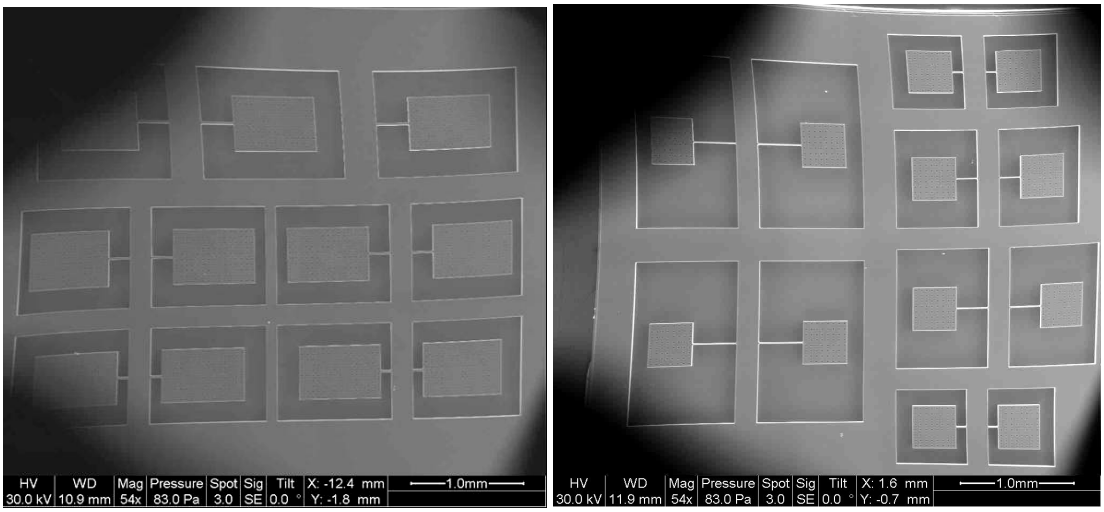

Figure 22. ESEM images of an in-plane type A die (left) and an in-plane type B die (right) that were subjected to a 3068g acceleration pulse

The figure above reveals that none of the shock test structures failed at lower stress levels caused by the 3068g acceleration pulse. Therefore, ESEM was performed on only the failed structures from the 5000g acceleration pulse drop test. Figure 23 below shows a number of etching anomalies at or near the crack initiation site of in-plane type B devices.

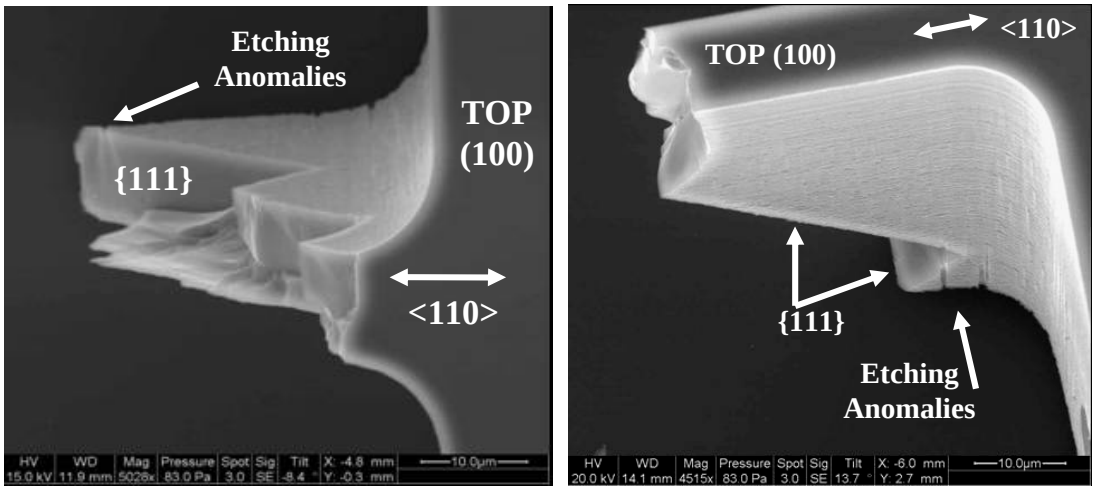

Figure 23. ESEM images showing structural failure of a 300µm in-plane type B shock test device (left) and a 200µm in-plane type B shock test device (right)

Figure 23 indicates that the cantilever beam failure resulted from cracks initiating at the side surface. This failure behavior was expected due to the applied in-plane bending load. In addition to etching anomalies such as those in Figure 23, post test inspections of structures from the 5000g shock test revealed that failures occurred along {111} planes. It is well known that materials containing diamond cubic structures fail on {111} planes because they are the weakest [13], [20]. Therefore, due to the diamond cubic crystal structure of single crystal silicon, the predominance of a {111} fracture plane was expected [20].

Out-of-plane Test Structures

As discussed above, the out-of-plane structures were initially subjected to an acceleration pulse of 5000g. All of the structures failed at this high acceleration level.

Therefore, a sequence of lower acceleration level tests was performed to create a range of fracture data on the devices.

After the initial 5000g test, the out-of-plane structures were subjected to acceleration pulses ranging from 1860g to 3070g along their critical loading direction using the Lansmont shock tower. A summary of these failures is below in Figure 12.

Table 9. Out-of-plane shock test summary

Acceleration	Max Dynamic Stress	Number of Devices Tested	Percent Failure
3,069g	1.58 GPa	4	100%
2,743g	1.23 GPa	4	100%
2,526g	1.13 GPa	8	88%
2,288g	1.03 GPa	8	63%
2,015g	0.87 GPa	11	36%
1,862g	0.80 GPa	8	25%
2,114g	0.93 GPa	8	38%
2,055g	0.90 GPa	8	63%
1,636g	0.70 GPa	12	25%

When these out-of-plane structures were subjected to acceleration pulses of 2740g and 3069g, all of the test structures failed. A die with 100% failed out-of-plane structures is shown in Figure 24.

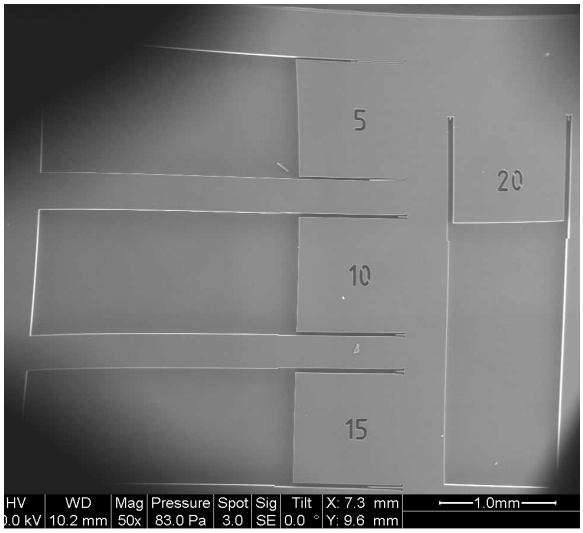

Figure 24. ESEM images of the single out-of-plane die that was subjected to a 3069g acceleration pulse

While Figure 24 shows a die with a 100% failure rate that resulted from a 3069g acceleration pulse, the following set of images show a set of die after a 2015g acceleration pulse. Unlike the die depicted in Figure 24, some structures did not fail at this lower acceleration level. Furthermore, three die were tested at this lower acceleration to provide a larger number of data points. The first two die contained a full set of four functional devices prior to testing. The third die, however, contained only three functional devices prior to testing. The device with a 20µ spacing between the cantilever and the side walls was stuck before the test and thus was not considered in the percent fracture calculation displayed in Table 9 above. The pictures in Figure 25 below show the results of this drop test. The devices with missing proof masses are marked as those that failed.

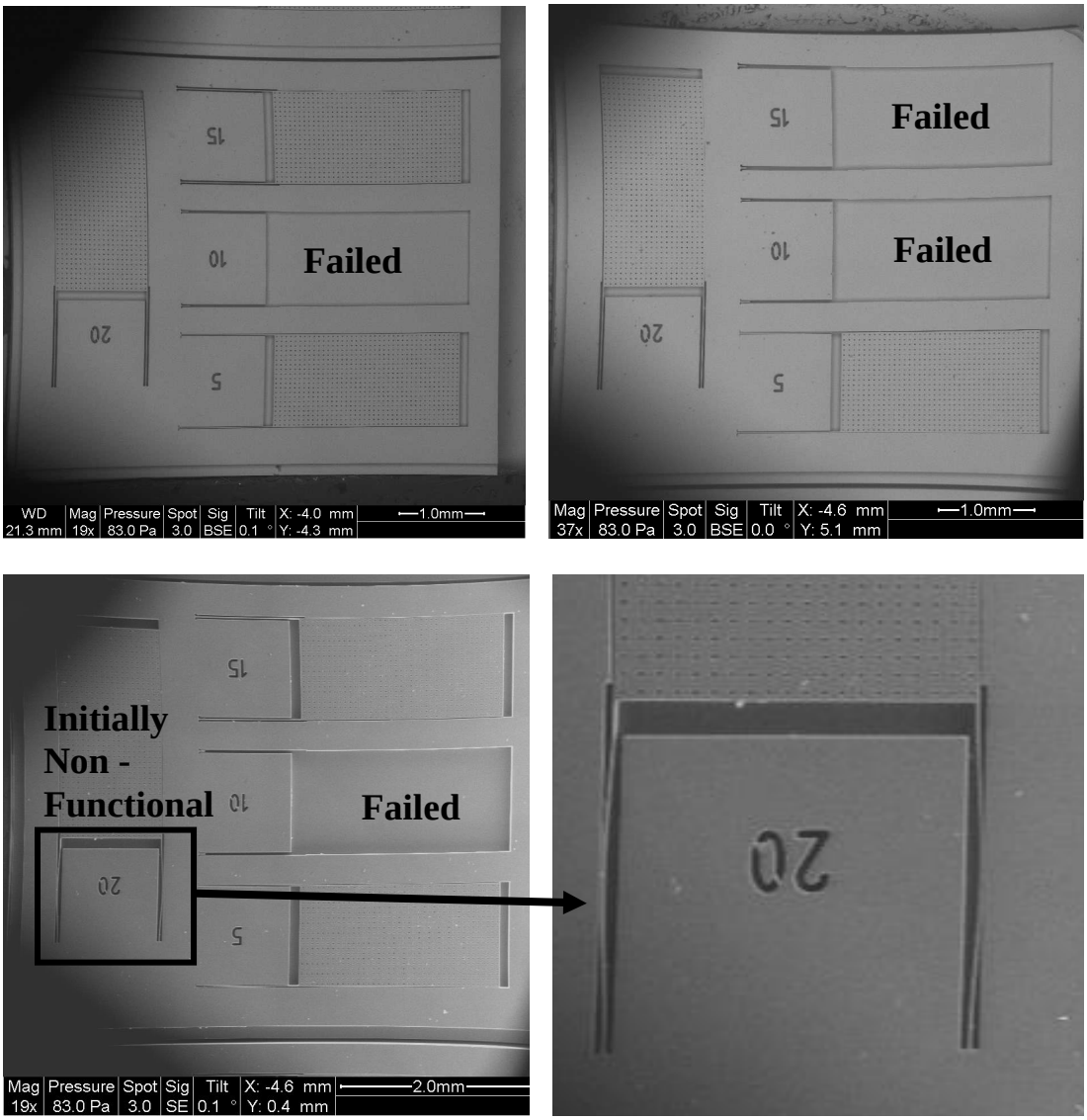

Figure 25. A set of out-of-plane dies exhibiting a 36% failure rate after being subjected to a 2015g acceleration pulse

Through examination of the bottom right photo in Figure 25, it is evident that the cantilever beams are stuck to the side walls for the 20µm device. ESEM photos of die from the other out-of-plane drop tests are in Appendix C.

Figure 26 illustrates an out-of-plane structure that failed near the wall support and that the failure propagated from the bottom surface of the beam to the top surface

of the beam, as expected for out-of-plane loading. This figure also indicates the failure occurred along a {111} plane. Both of these occurrences were very common with the out-of-plane devices.

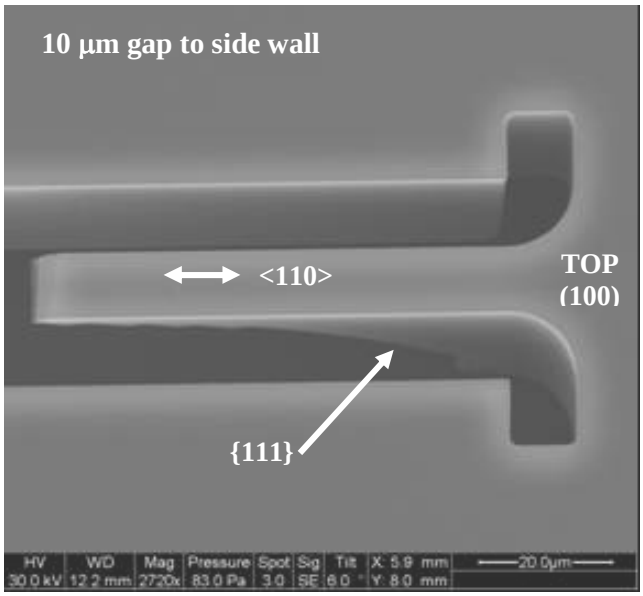

Figure 26. Structural failure ESEM images of an out-of-plane shock test device

Figure 27 shows the bottom surface of an out-of-plane cantilever beam that failed from a 2,526g drop test. The figure also suggests that the cracks may have initiated at locations where etching anomalies were present.

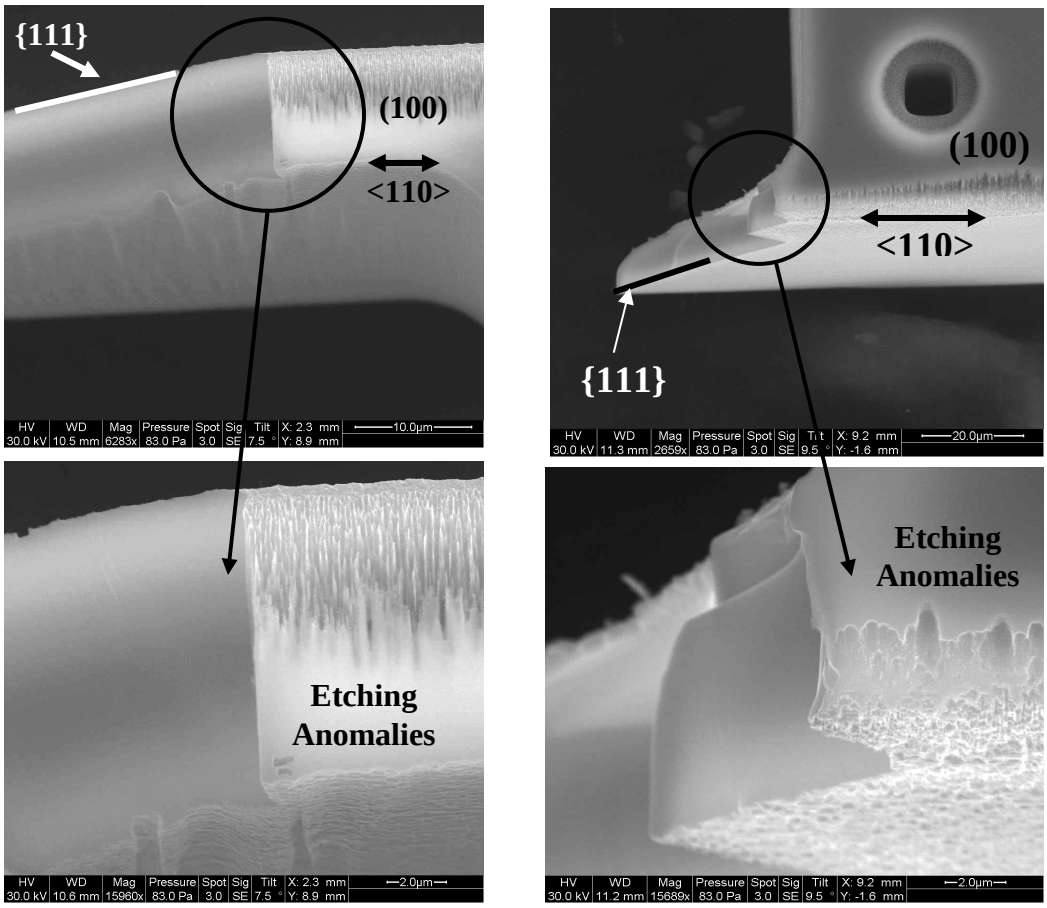

Figure 27. ESEM images showing etching anomalies at the bottom surface of a cantilever beam that failed from a 2526g drop test (left) and a 2288g drop test (right**).**

As described by Table 9, a large number of out-of-plane devices were tested at various accelerations. The wide range of fracture percentages that resulted from these drop tests indicates a strong correlation between failure and maximum acceleration level. This relationship is examined and quantified further in the following section.

Discussion

The majority of the results presented above were expected, with the number of failed out-of-plane samples increasing as the applied acceleration increased. However, an unexpected observation occurred during the 5000g test of the in-plane structures. Although the longest cantilever structures experience the highest stress for any given acceleration, during this test the shortest cantilever structures failed while devices with longer cantilevers remained intact.

One possible reason for the unexpected failures of the in-plane structures is that the proof-masses attached to the longer cantilevers were hitting the side walls, thus preventing maximum stress levels from being reached. By multiplying the maximum static deflections by a factor of 2, the worst-case estimates of dynamic deflection for the longest type A and type B structures were calculated as 105µm and 251µm, respectively. Both of these values are much smaller than the corresponding gap distances of 250µm and 550µm. It is therefore unlikely that the unexpected failures were caused by proof-masses hitting the side walls. An alternative explanation involves excitation of the in-plane structures at or near their resonance frequencies.

While the lower acceleration time history plots did not contain a large amount of noise, the time history plots of the 5,000g pulses suggest that the structures experienced high-amplitude and high-frequency vibrations for several milliseconds after the initial loading. A comparison of a 3,000g pulse and a 5,000g pulse was shown in Figure 8.

From examination of Figure 8, it is clear that the 5,000g drop test contained a significant amount of high amplitude peaks after the initial 5,000g loading. The 3,068g drop test, on the other hand, was a very clean pulse and contained minimal amplitude peaks after initial loading. The significant differences in frequency content of these tests and the varying failure results motivated a study involving modal analysis of the in-plane structures.

To determine the frequency content of the acceleration pulse, a Fast Fourier transform (FFT) of the time history plot was performed on the 5,000g pulse. The resulting FFT indicated peak frequency content at 9.57 kHz, 10.64 kHz, and 12.34 kHz. The FFT plot is below in Figure 28.

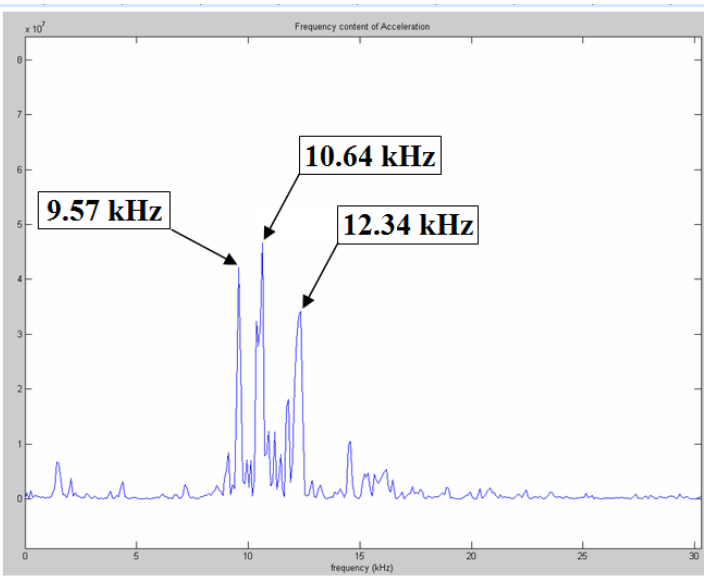

Figure 28. FFT of 5,000g acceleration pulse [14]

As depicted in Table 6, the first natural frequency for the shortest cantilever type A device is 11.32kHz and for the shortest cantilever type B device is 10.39 KHz. These frequencies are relatively close to peaks in the FFT plot shown above.

Therefore, it was concluded that the high frequency content of the 5,000g pulse induced resonance in the shortest in-plane devices, causing them to fail. This reasoning also explains why the longer cantilever beams with higher calculated stresses, but unmatched natural frequencies, did not fail.

The FFT study showed that the in-plane device failures at 5,000g were not a result of exceeding the strength of single crystal silicon but were instead from excitation of their resonant frequencies. Dynamic stress calculations on the 5,000g acceleration pulse demonstrated the maximum stress experienced by the in-plane structures was 1.1 GPa. Because none of the devices subjected to this stress level failed during testing, it was concluded that the dynamic fracture strength of DRIE processed single crystal silicon is greater than 1.1 GPa for bending around the <100> directions. Further testing at higher acceleration levels or with redesigned shock structures will be required to collect failure data for bending around the <100> directions. This will be discussed in the subsequent section on recommendations for future work.

The behavior of the out-of-plane structures was as expected, with the percentage of failed devices increasing as the maximum dynamic stress increased. Although structures with different gap distances between the cantilever beams and the side walls were tested, no correlation was found between device failure and gap width.

In order for shock test structures to be excited, their shock amplification factors must be larger or equal to 1. By examination of Figure 12, it is evident that for a half sine wave, a shock amplification factor of 1 corresponds to a shock

parameter value of about 0.45. Therefore, shock parameter values were calculated to ensure that they were greater than 0.45. For all of the drop tests, shock parameter values were found to be between 1.09 and 1.29. This indicates that the test structures were excited and thus subjected to dynamic shock loading during drop tests.

Although the in-plane structures did not fail at even the maximum stress levels to which they were subjected, the out-of-plane devices did show visible failure when subjected to high acceleration drop tests. The data collected from out-of-plane shock testing experiments contained both left and right suspended (censored) units. For left censored data, the interval within which the failure occurred is known. However, the exact stress level at failure is not known. The devices that failed during shock testing are an example of left censored data. In the Webiull analysis performed, it was assumed that the devices failed at the maximum stress values they experienced during testing. For right censored data, the unit is removed from testing before failure occurs, as is the case for all devices that did not break during testing. To overcome the obstacles associated with right censored data, a suspended and grouped data analysis using Weibull ++ software was performed. The Weibull plot showing the results of the out-of-plane structure drop tests is shown below in Figure 29.

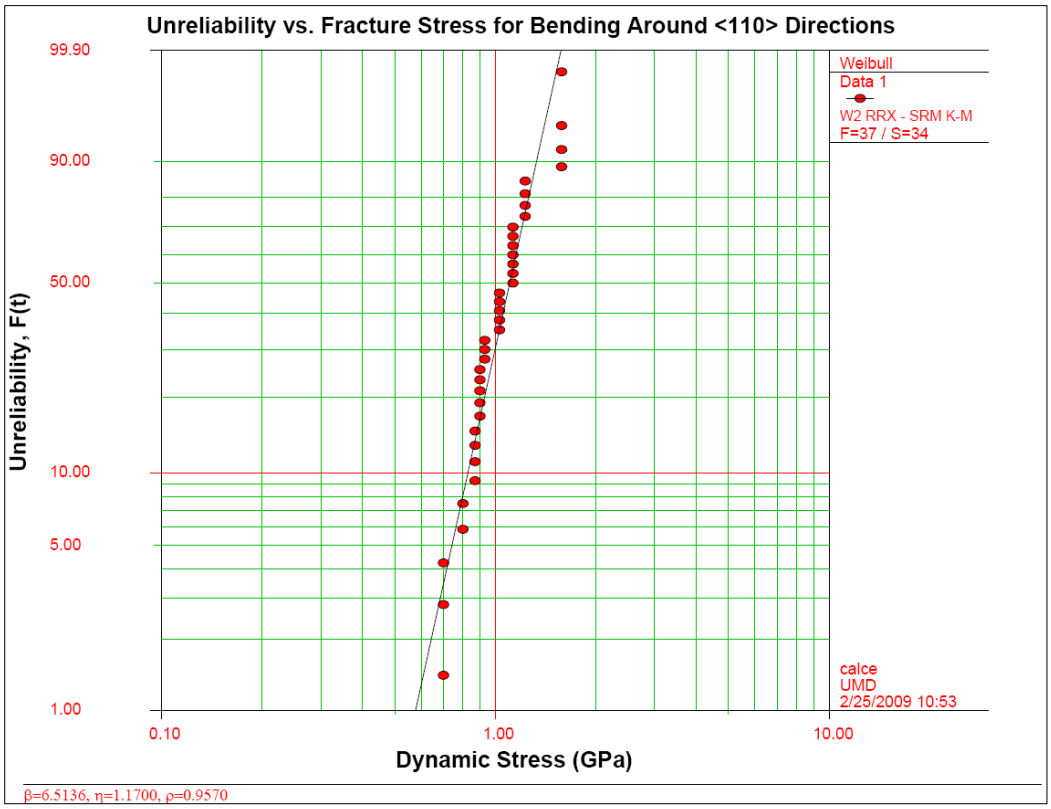

Figure 29. Weibull plot of out-of-plane device failures

To take into account data points representing both failed and intact structures, a data point for each structure tested was inserted into the Weibull ++ program. Therefore, four data points were listed for each 100% functional die. Traditional Weibull plots measure reliability on the y-axis and a time to failure metric on the x-axis. To represent the shock data gathered, however, the maximum dynamic stress level was used as the independent variable on the x-axis. It is important to note that because the plot above is untraditional in the sense that in does not involve a time to failure metric and that it contains suspended data, the Weibull parameter values are not likely to be significant indicators of data trends or failure modes.

The dynamic stress values listed in the Weibull plot above are for the bending of DRIE processed SCSi around the <110> direction. This Weibull distribution is a tool that can be used to determine the maximum dynamic stress to which a device can be subjected in order to achieve a specific reliability goal. This will allow designers to use modeling and virtual qualification to build and incorporate new MEMS devices into current technologies without time intensive and costly testing.

Chapter 5: Conclusions, Contributions, and Future Work

Conclusion

As discussed in the literature review, extensive research has been performed to determine the quasi-static fracture strength of single crystal silicon. An enormous amount of variability was found to occur because of the different processing steps used to fabricate test samples. Some examples of factors that have been found to significantly affect the quasi-static fracture strength of single crystal silicon include wafer coatings, annealing procedures, etchant composition and type, and the size of the test sample. In order for MEMS designers to use these values to create meaningful models and perform verification studies, a database that documents these various fracture strengths and test conditions must be generated.

Although many tests have been performed to determine the quasi-static fracture strength of single crystal silicon, very little research has been performed to investigate the effect of high acceleration, dynamic loading on the material. Many military devices that contain electronics and MEMS strucutres are subjected to extremely high accelerations upon launching. Even commercial devices, such as cell phones and handheld PDAs, can experience high shock loads if they are dropped from common heights onto hard surfaces. The current protocol used to determine the ruggedness of devices facing these types of high shock loads is “pass-fail” testing during which the device is checked for functionality following a given number of drops. Unfortunately, this is both time consuming and expensive.

A testing method that provides dynamic fracture strength values for MEMS devices made from single crystal silicon has been developed and demonstrated. This testing method is very simple and straightforward, requiring little setup and nearly trivial fabrication process steps. Through use of a drop tower and an accelerometer, single crystal silicon devices can be tested to find the dynamic fracture strength for bending around various directions. Because of the ease with which this method can be carried out, it is a good tool to examine the affects of various processing techniques commonly performed to produce MEMS devices.

In addition to developing a method to subject these small microscale structures to dynamic loading conditions, a simple test specimen geometry that allows for straightforward analytic calculations of fracture stress was presented. The maximum static fracture stress of the cantilever and proof mass structures was determined through the application of static beam equations. Sloan's equations for undamped, single degree of freedom spring mass systems were then used to find a shock amplification factor, which is multiplied by the static stress to provide a dynamic stress value. By cross checking the results of these calculations with the results of dynamic FEA simulations, it was confirmed that the analytic dynamic fracture strength values are accurate and the method used to determine them is acceptable.

For the in-plane samples tested, a fracture distribution could not be created due to the limitations of the shock towers available for this research. However, it was determined that the dynamic fracture strength of DRIE processed (100) single crystal silicon is greater than 1.10 GPa for bending around <100> directions. In order to

create a fracture strength distribution for bending around the <100> directions, the in-plane samples need to be redesigned and tested.

A dynamic strength Weibull distribution was created for DRIE processed (100) single crystal silicon for bending around <110> directions using the out-of-plane test samples. This distribution is an important tool that will allow MEMS designers to determine the maximum stress to which a component can be subjected in order to achieve a desired reliability value.

As discussed in the literature review, a large range of quasi-static fracture strength values have been reported. These values range from 0.3 GPa to over 4.6 GPa and vary significantly with sample size and processing technique. The group at the University of Heidelberg also reported the dynamic stress for crack nucleation in bulk single crystal silicon to be between 5-7 GPa. Unfortunately, due to the lack of information in these research papers on test structure processing conditions, fracture planes, and loading directions, it is challenging to compare the dynamic fracture strength values found in this analysis to those found in prior work. This underscores the need for detailed documentation of test setup and sample preparation in order to create a meaningful and valuable database of fracture strength values for device designers.

The shock test method presented is a simple, inexpensive, and accurate process that results in dynamic fracture strength values. The out-of-plane bending results, along with others that come about from future implementation of this shock test method, can be used for modeling and virtual qualification of both military and commercial products.

Contributions

The contributions from this project are as follows:

- An economical and efficient dynamic testing method to find dynamic fracture strength of DRIE processed single crystal silicon is presented
- Verification of this testing method has been performed by subjecting shock structures to bending around the <100> and <110> directions

Future Work

As described in the results and discussion sections, further testing of the in-plane devices is required to create a dynamic stress distribution similar to the Weibull plot presented for the out-of-plane structures. Because this Weibull plot will be an important tool for device designers, it is important that further testing of the in-plane devices is performed accurately and that the results are repeatable.

Previous discussion regarding the two different shock tower systems demonstrated that the larger shock system resulted in high frequency content, "noisy" pulses whereas the smaller Lansmont system provided much cleaner pulses. Analysis of the in-plane tests results revealed that in order to prevent excitation of the structures' resonant frequencies, a clean pulse was required. Unfortunately, the in-plane devices did not fail when subjected to a 5,000g pulse and accelerations any higher than this would include a significant amount of high frequency noise. Therefore, it was concluded that the in-plane test structures needed to be redesigned so that they can be tested and failed at a lower acceleration with a clean pulse.

The objectives of the in-plane test structure redesign can be achieved in many ways, including decreasing the cantilever width, decreasing the thickness of the test structures, increasing the size of the proof mass, elongating the cantilever beams, etc. The two redesign methods that are currently being considered represent straightforward techniques that should not be challenging to implement during fabrication. These involve increasing the size of the proof mass and increasing the length of the cantilever.

Although dynamic stress is the primary concern in this project, static stress values were used to compare devices in the redesign study. The reason for the use of static stresses is that they are a good indicator of dynamic stress and can be found through straightforward calculations. To determine dynamic stresses from these static values, the acceleration pulse width, natural frequency, and maximum acceleration level must be known. The maximum acceleration and pulse width, however, cannot be determined until shock testing takes place. Nevertheless, the strong, direct correlation between static and dynamic stress allows for conclusions to be made regarding the effect of changing the geometries of the in-plane structures. Detailed calculations on the effects of these redesign options can be found in Appendix D.

The redesign studies of the in-plane type-A and type-B devices demonstrate that either increasing cantilever length or increasing proof mass size will result in structures that experience significantly larger maximum stresses than they experienced in previous drop tests. Therefore, a combination of both increased cantilever length and increased proof mass size will likely be implemented in the redesign of the in-plane structures. The desired outcome of an in-plane structure redesign is that the devices will fail within the limitations of the Lansmont drop tower and that a dynamic fracture strength distribution can be generated. Therefore, it is recommended that future work involves performing a statistically significant number of drop tests with these redesigned structures and creating a Weibull distribution to represent the results of these tests.

In addition to the further testing of the DRIE etched in-plane samples, future work should be performed to examine the effect of different etchants, processing

techniques, and structure size scales on dynamic fracture strength for bending around various single crystal silicon directions. The results of such studies could then be compared the previously determined quasi-static fracture strength values to determine what, if any, relationship exists between the dynamic and quasi-static mechanical properties of single crystal silicon.

Appendix A

Critical Loading Direction MATLAB Calculations for out-of-plane devices

```
% Out of Plane

clc
clear
close all

rho = 2330;                         % kg/m^3
E = 169 * 10^9;                     % N/m^2
t = 100 * 10^-6;                    % Device Layer Thickness in m
a = 2288.04 * 9.8;                     % a = 5000 g in m/s^2

nl = 40;                             % # holes along x direction
nw = 20;                             % # holes along Y direction
section_length = 50 * 10^-6;          % m
hole_in_section_length = 10 * 10^-6;          % m
section_mass = ((section_length)^2 - (hole_in_section_length)^2) *
rho * t;  % kg
proof_mass = nl * nw * section_mass;                                % kg
Length_proofmass = nl * section_length;          % m

F_a = proof_mass * a;              % Where F_a is the applied force
in N
F_each_side = F_a/2;
M_each_side= (F_each_side) * Length_proofmass/2;     % N-m
L = 1000 * 10^-6;                   % Length of cantilever

w = 10 * 10^-6;                    % Width of cantilever in m
Iy = (1/12) * t^3 * w;             % Moment of Inertia (Iy) for
cantilever beams m^4
M_r = F_each_side * L + M_each_side;              % Reaction moments
in N-m

sigma_static_in_GPa = (M_r * (t/2) / Iy)*10^-9   % IN GPa
% theta_p = - F_a * L^2 /(2*E*Iy) - M_a * L /(E*Iy); % radians
% delta_p = - F_a * L^3 /(3*E*Iy) - M_a * L^2 /(2*E*Iy);        % m
% delta_proofmass_static = delta_p + L_m * sin(theta_p);        % m
```

Critical Loading Direction MATLAB Calculations for in-plane Type A devices

```
% In plane Type A

clc
clear
close all

rho = 2330;                         % kg/m^3
E = 169 * 10^9;                     % N/m^2
t = 100 * 10^-6;                    % Device Layer Thickness in m
a = 3000 * 9.8;                     % a = 5000 g in m/s^2

nl = 15;                            % # holes along X direction
nw = 10;                            % # holes along Y direction
block_length = 50 * 10^-6;          % m
hole_length = 10 * 10^-6;           % m
block_mass = ((block_length)^2 - (hole_length)^2) * rho * t;  % kg
proof_mass = nl * nw * block_mass;                            % kg
L_m = nl * block_length;            % m

F_a = proof_mass * a;               % N
M_a = proof_mass * a * L_m/2;       % N-m

% L = 300 * 10^-6;                  % Length of cantilever in m
% L = 200 * 10^-6                   % Length of cantilever in m
% L = 100 * 10^-6                  % Length of cantilever in m

w = 20 * 10^-6;                     % Width of cantilever in m
Iz = (1/12) * t * w^3;              % m^4
M_r = F_a * L + M_a;                % N-m

sigma_static = M_r * (w/2) / Iz  % N/m^2
theta_p = - F_a * L^2 /(2*E*Iz) - M_a * L /(E*Iz);          %
radians
delta_p = - F_a * L^3 /(3*E*Iz) - M_a * L^2 /(2*E*Iz);      % m
delta_proofmass_staitc = delta_p + L_m * sin(theta_p);      % m
```

Critical Loading Direction MATLAB Calculations for in-plane Type B devices

```
% In plane Type B

clc
clear
close all

rho = 2330;                         % kg/m^3
E = 169 * 10^9;                     % N/m^2
t = 100 * 10^-6;                    % Device Layer Thickness in m
a = 3000 * 9.8;                     % a = 5000 g in m/s^2

nl = 8;                             % # holes along X direction
nw = 8;                             % # holes along Y direction
block_length = 50 * 10^-6;          % m
hole_length = 10 * 10^-6;           % m
block_mass = ((block_length)^2 - (hole_length)^2) * rho * t;   % kg
proof_mass = nl * nw * block_mass;                             % kg
L_m = nl * block_length;            % m

F_a = proof_mass * a;               % N
M_a = proof_mass * a * L_m/2;       % N-m

% L = 400 * 10^-6;                    % Length of cantilever in m
% L = 300 * 10^-6;                  % Length of cantilever in m
% L = 200 * 10^-6;                  % Length of cantilever in m
L = 500 * 10^-6;                  % Length of cantilever in m

w = 10 * 10^-6;                     % Width of cantilever in m
Iz = (1/12) * t * w^3;              % m^4
M_r = F_a * L + M_a;                % N-m
sigma_static = M_r * (w/2) / Iz                            % N/m^2
theta_p = - F_a * L^2 /(2*E*Iz) - M_a * L /(E*Iz);           % radians
delta_p = - F_a * L^3 /(3*E*Iz) - M_a * L^2 /(2*E*Iz);       % m
delta_proofmass_staitc = delta_p + L_m * sin(theta_p);       % m
```

Appendix B

Study on the effect of notching on MEMS shock tests

It has been demonstrated in previous work that excitation of a test system does not occur when the natural frequency of the test sample corresponds to the frequency at which a notch in a shock spectrum of a half sine pulse is found [F]. These notches in the shock spectrum are evident as the relative minima found in figure 12. A study was performed to determine the influence of this notching, or excitation suppression, on the MEMS test samples.

Notches occur at a frequency w, which can be found through the equation:

$$w = w_o(2k+1) \qquad \text{where K is an integer} > 1$$

In the equation above, $w_o = \pi/t_o$ where t_o is the pulse duration in seconds. By converting w from radians into hertz, the natural frequency of the test devices and the frequency at which the notches occur can be compared. The table below shows results from the notch calculations performed on the MEMS drop tests. Note that the numerical subscripts on the "w" terms represent the conditions where k=1, k=2, k=3, etc.

Table 10. Calculations to determine frequencies at which notching occurs

Max Acceleration (g)	Pulse Width (sec)	w_o (hz)	k	Notch Frequencies (hz)		
				w_1	w_2	w_3
5,000	2.8E-04	1,786	1	5,357	8,929	12,500
3,000	4.1E-04	1,220	2	3,659	6,098	8,537
2,743	4.5E-04	1,111	3	3,333	5,556	7,778
2,526	4.5E-04	1,111	4	3,333	5,556	7,778
2,288	4.5E-04	1,111	5	3,333	5,556	7,778
2,015	5.1E-04	980	6	2,941	4,902	6,863

1,862	5.2E-04	962	7	2,885	4,808	6,731
2,114	4.8E-04	1,042	8	3,125	5,208	7,292
2,055	4.9E-04	1,020	9	3,061	5,102	7,143
1,636	5.3E-04	943	10	2,830	4,717	6,604

The table below lists the natural frequencies for each of the test samples.

Table 11. Natural frequencies for MEMS shock test devices

Device	**Cantilever Length (μm)**	**f_n (Hz)**
Out-Of-Plane	1000	2,378
In-Plane Type A	100	11,318
	200	7,406
	300	5,578
In-Plane Type B	100	10,387
	200	6,369
	300	4,550
	400	3,486

Although the natural frequencies of some of the test samples seem to be relatively close to the frequencies at which notches occur, no evidence of excitation suppression was found in the test results. This may be due to the fact that these notching equations are for a perfect half sine wave while our acceleration pulses contain noise and damping. Furthermore, because a large number of different drop tests were performed and the acceleration pulses had varying pulse durations, the effect of notching, if any, is assumed to be negligible in the context of this research project.

Appendix C

This section includes information on the drop tests performed. For each test, the acceleration pulse is presented. In addition to the accelerometer data, ESEM pictures showing the structures after testing are displayed.

2743g Maximum Acceleration Pulse

A single die containing out-of-plane structures was subjected to an acceleration of 2743g. The acceleration curve for this drop test is shown below:

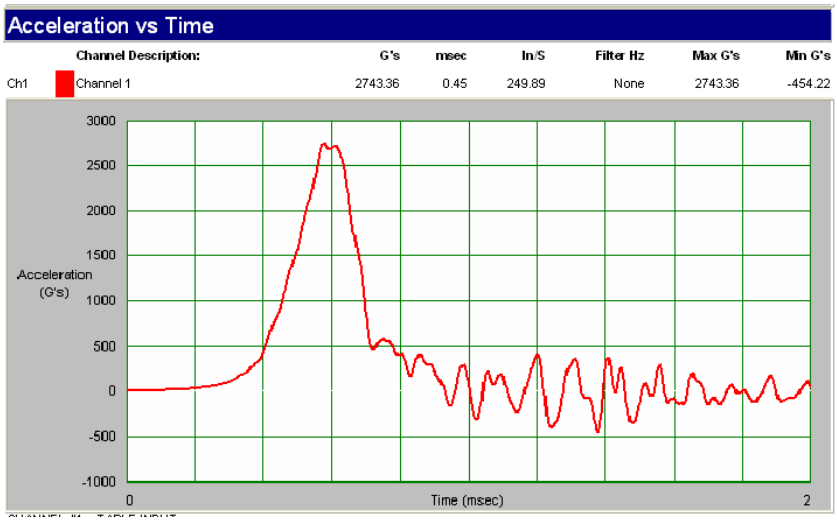

Figure 30. 2743g acceleration pulse profile

For the block one structures, the maximum stress occurs at the wall support of the cantilever beams. The shock amplification factor for the pulse shown above was determined to be 1.71 and thus the maximum dynamic stress value was 1.231 GPa. The following image shows that all of the block one devices broke during this test.

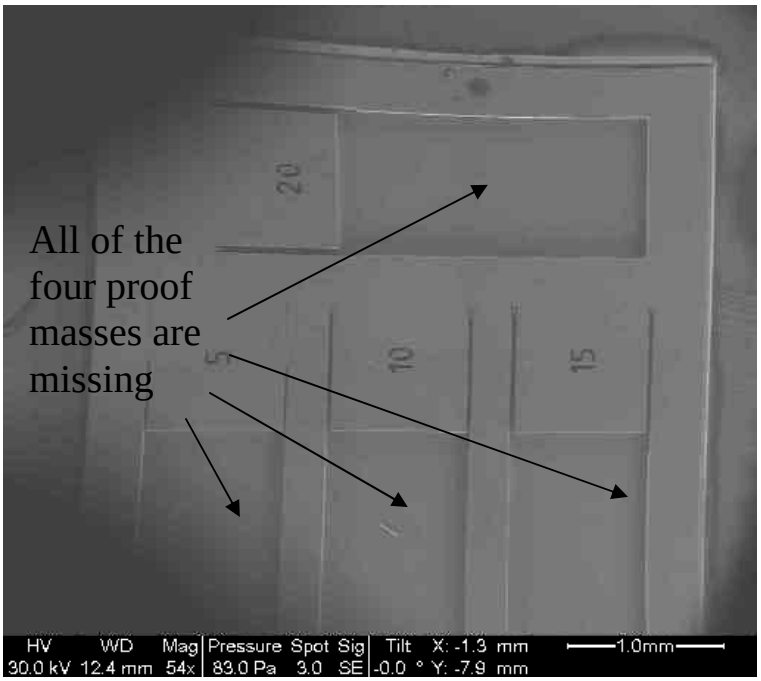

Figure 31. Results of 2743g drop test

In addition to determining whether the devices broke, pictures of the fracture sites were taken to examine where and how the cracks were formed. The two pictures shown below are the two fracture sites on the test structure with a 15 micron spacing between the wall and the cantilever. These images show that the fractures both occur along (111) planes.

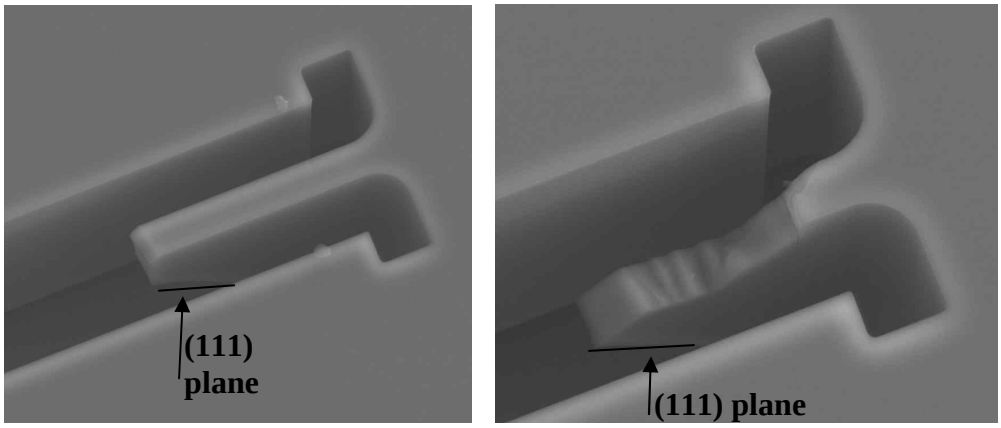

Figure 32. Fracture sites on the 15µm device after a 2743g drop test

Although the fracture sites on the proof masses were examined, unfortunately the proof masses could not be matched with the fracture sites of the individual test structures because tiny intermediate pieces of cantilever broke off during testing and could not be recovered.

2526g Maximum Acceleration Pulse

Two sets of out-of-plane structures were subjected to an acceleration of 2526g. At this acceleration, these devices experienced a maximum dynamic stress level of 1.133Gpa. The pulse is shown below:

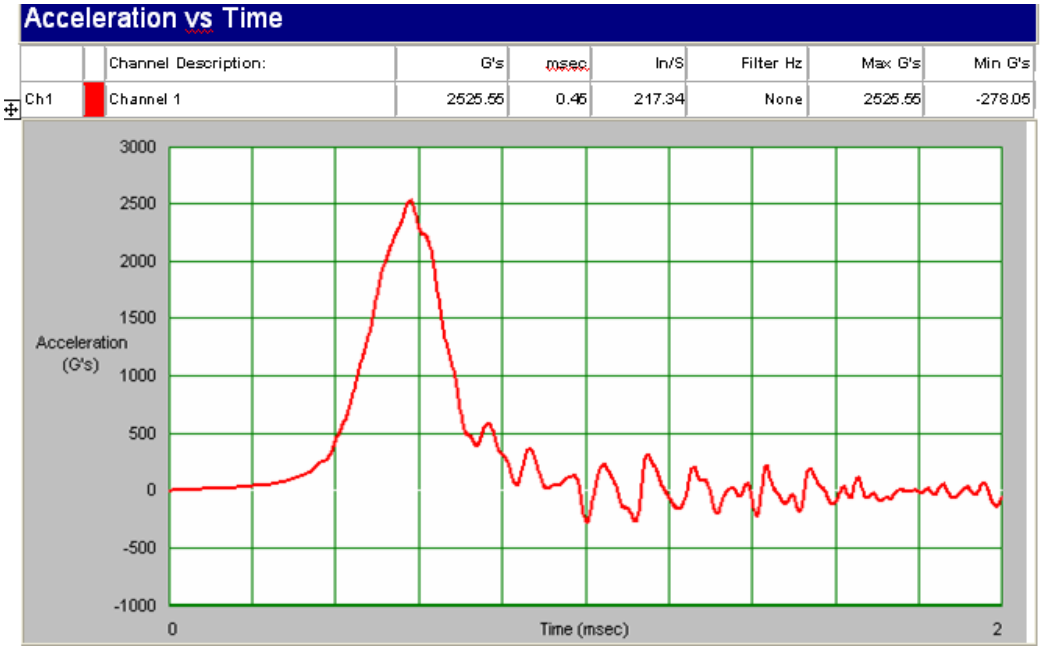

Figure 33. 2526g acceleration pulse profile

The result of this drop test was that all but one structure failed. The picture below is of the first set of out of plane structures. In this die, every proof mass failed.

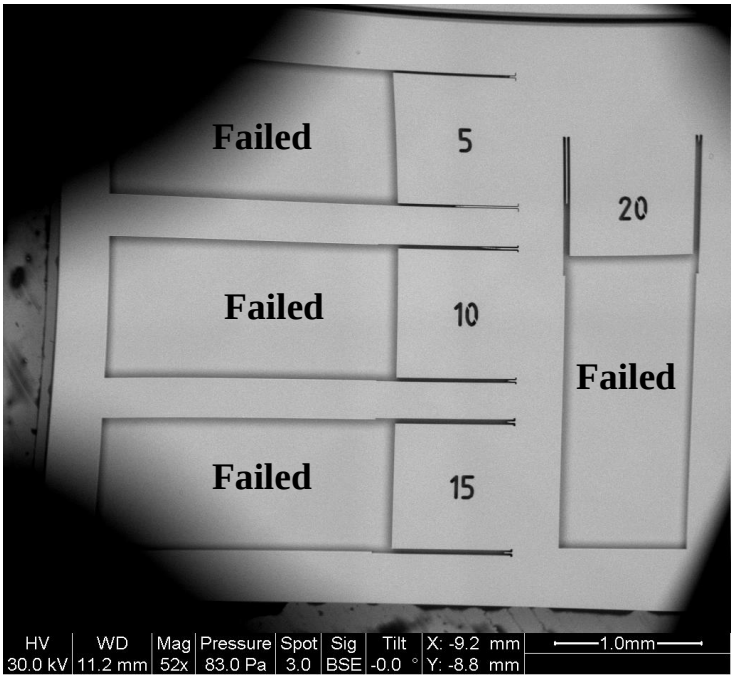

Figure 34. One of the die testing during the 2526g drop test

The following picture shows the second set of devices tested in which one proof mass remained attached. The device with 20 micron spacing between the cantilevers and the side walls did not fail. Therefore, the proof mass on this device can be seen below while the other proof masses are missing.

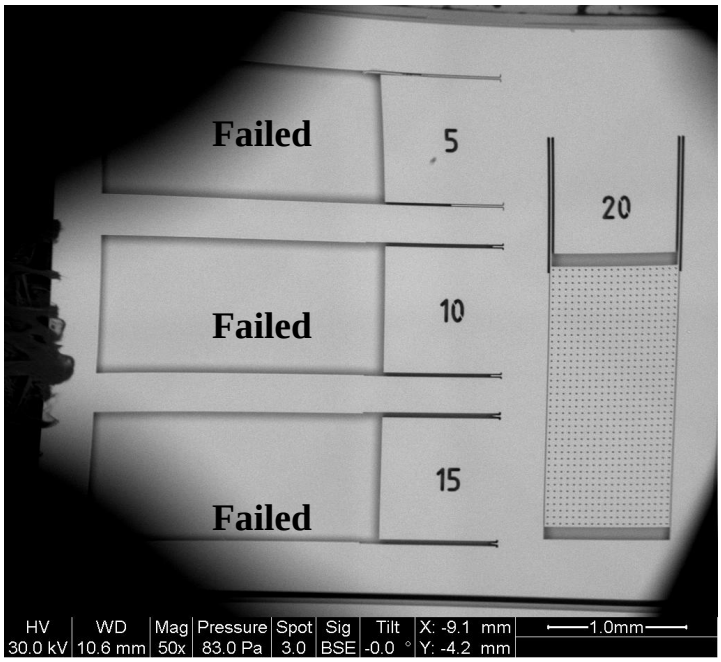

Figure 35. The second die testing during the 2526g drop test

Upon examination of the proof masses that broke away from the devices during testing, it was found that again, fractures occurred along the <111> plane.

2288g Maximum Acceleration Pulse

A set of two die were tested at an acceleration of 2288g and experienced a maximum dynamic stress of 1.027GPa. The acceleration pulse from this test is shown on the following page.

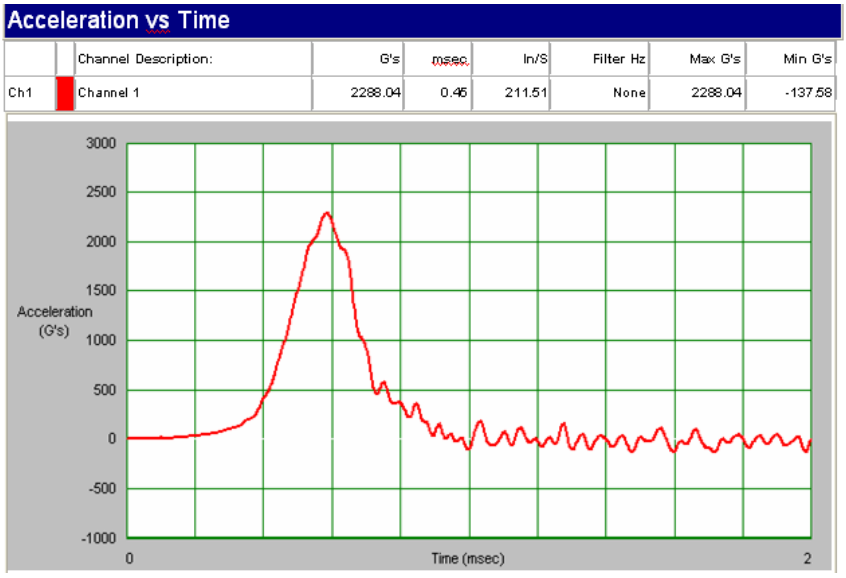

Figure 36. 2288g acceleration pulse profile

During this test, only five out of eight devices broke. The pictures below show the two sets of devices after testing.

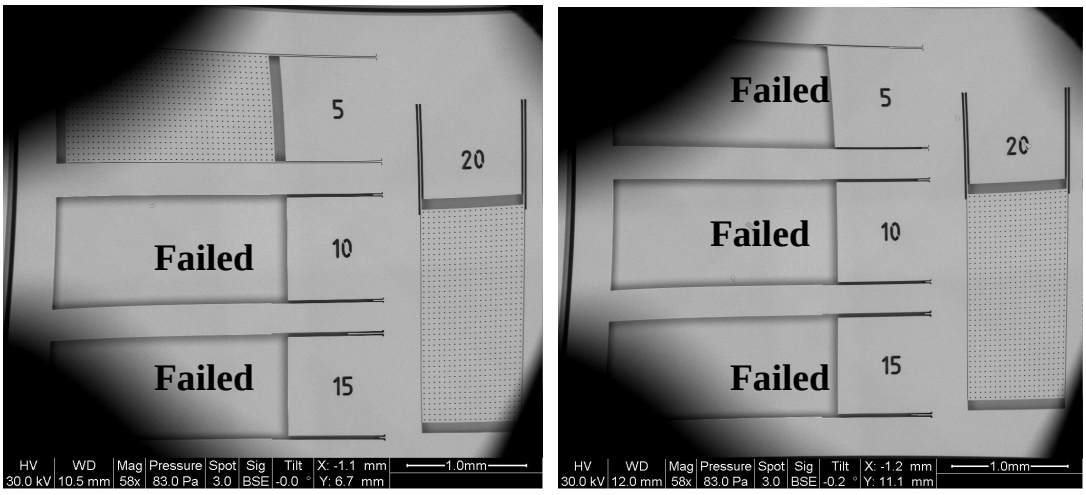

Figure 37. Out-of-plane devices after a 2288g maximum acceleration pulse

Similarly to previous tests, fractures from the 2288g drop test occurred along the <111> plane as shown in the picture below. This picture shows the site of initial crack propagation on one of the proof masses.

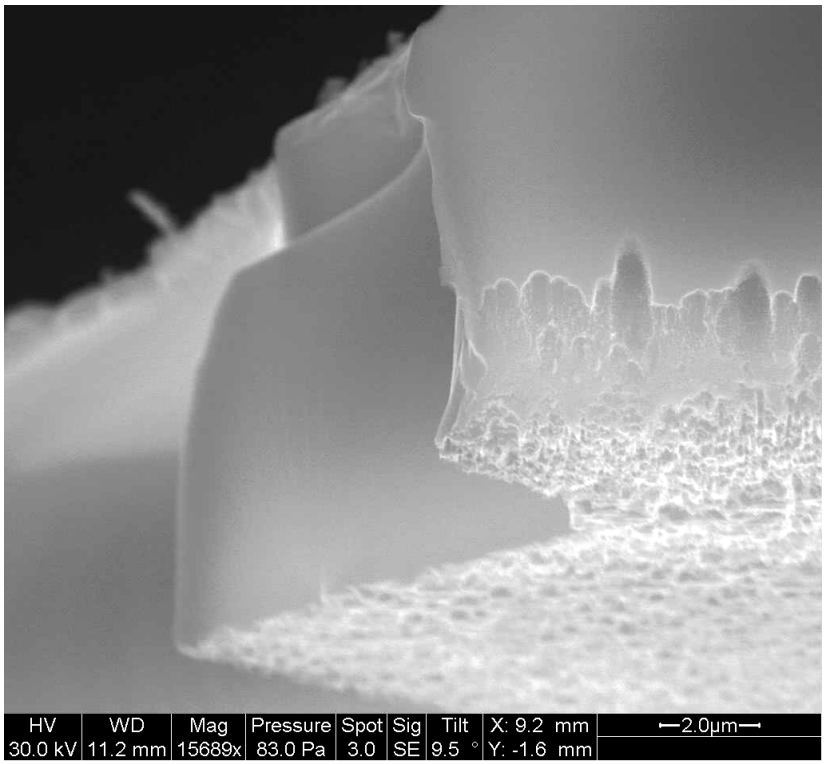

Figure 38. Exposed <111> fracture planes on out-of-plane device after testing

1862g Maximum Acceleration Pulse

A set of two die were tested at an acceleration of 1862g and experienced a maximum dynamic stress of 0.793GPa. The acceleration pulse from this test is shown below.

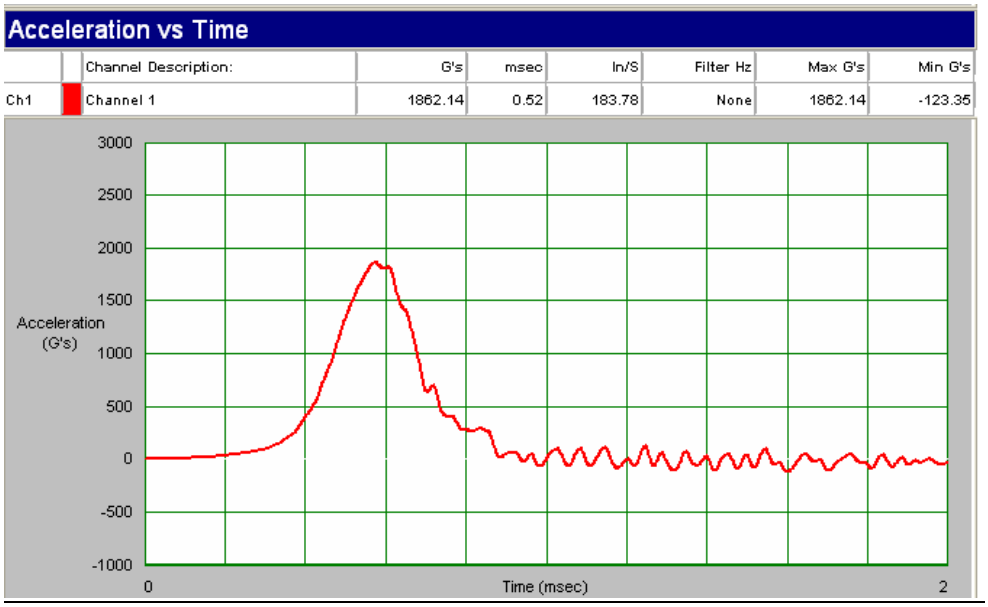

Figure 39. 1862g acceleration pulse profile

This test sample contained two die. In each die, the device with a 10µ spacing between the cantilever and side walls broke. This is pictured below.

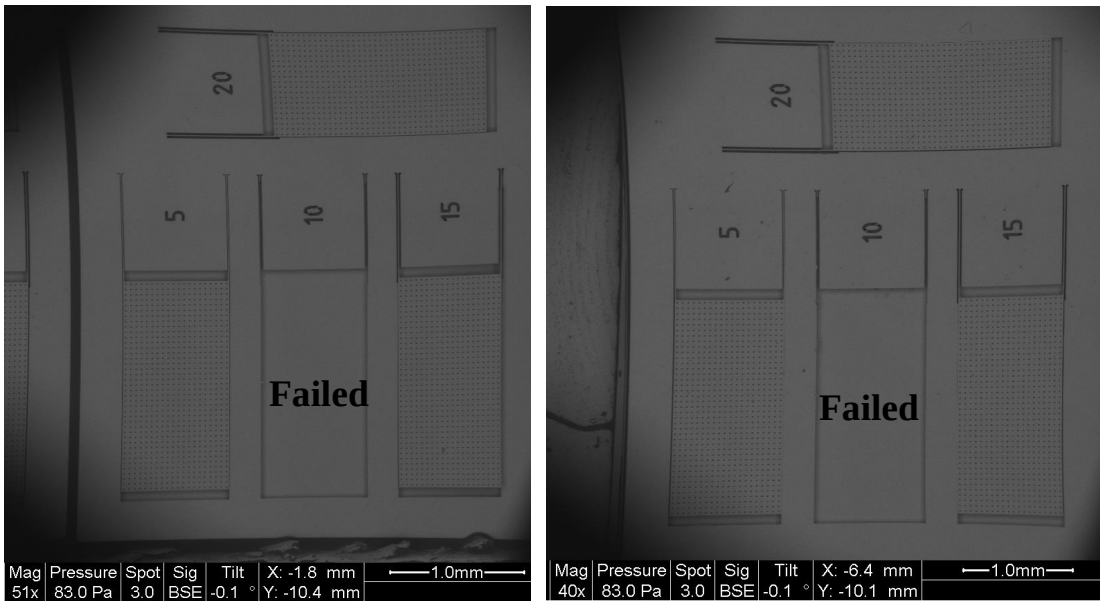

Figure 40. Results of 1862g maximum acceleration pulse

The following two pictures show the sites of fracture at the base of the devices that broke during testing. As predicted from maximum stress calculations, the fractures occur close to the cantilever supports.

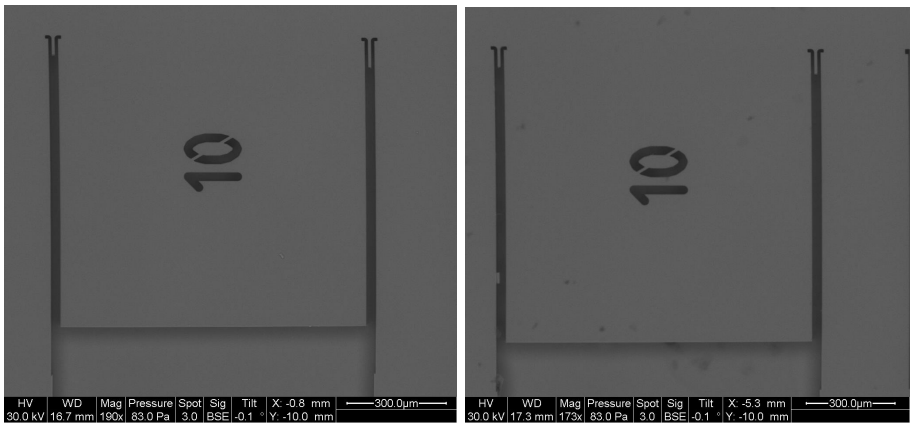

Figure 41. Two different fracture sites near the wall support

2015g Maximum Acceleration Pulse

This test involved three die, each containing 4 devices. The acceleration pulse and images of the MEMS structures after the drop test are below.

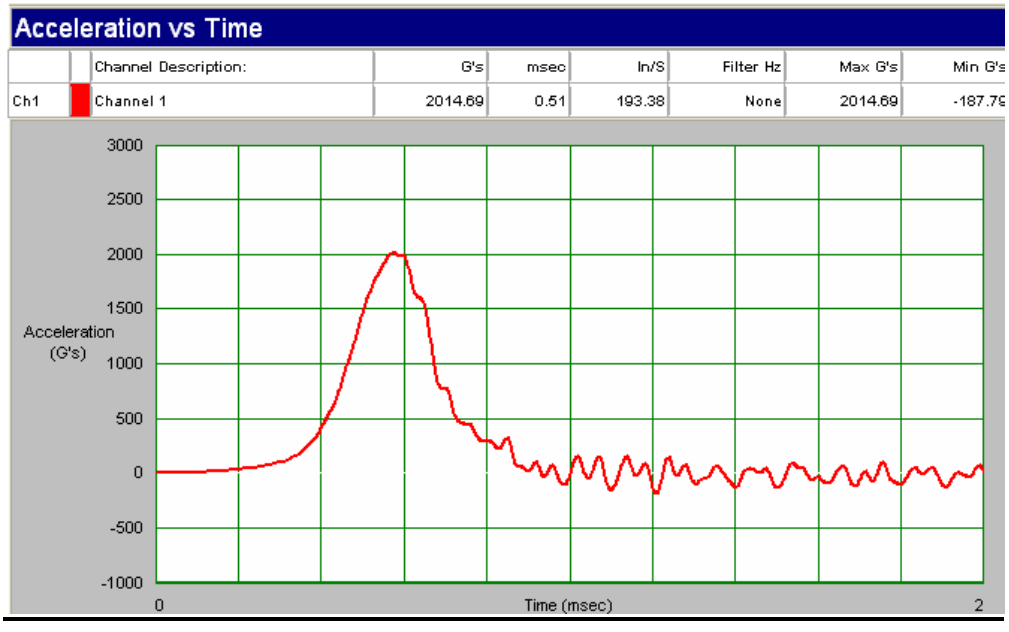

Figure 42. Acceleration Pulse for 2015g drop test

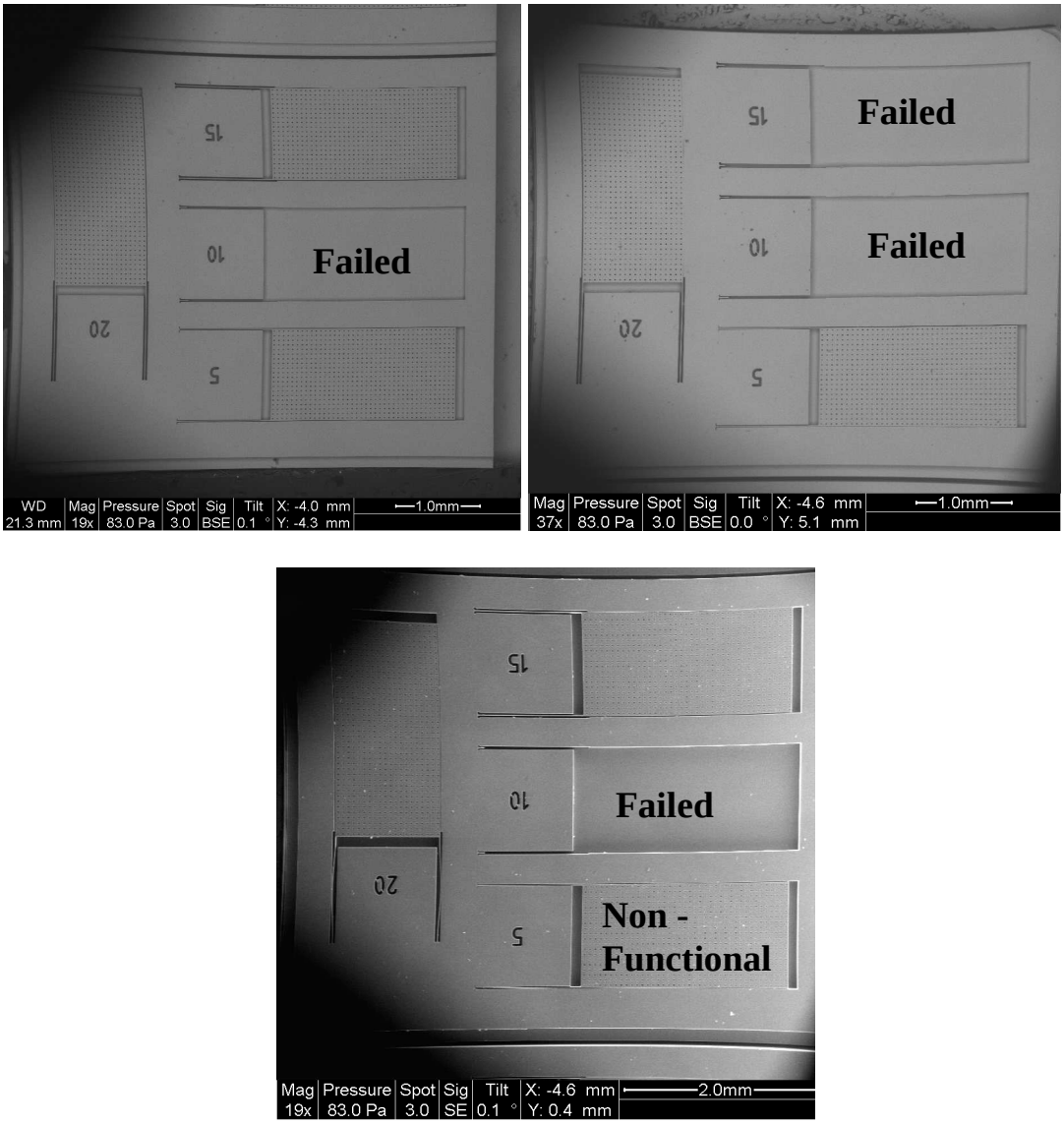

Figure 43. Images of the structures after a 2015g drop test

The third block of structures contained only three functional devices prior to testing. The device with a 20µ spacing between the cantilever and the side walls was stuck before the test and thus was not considered in the percent fracture calculation discussed above.

2114g Maximum Acceleration Pulse

Two die were subjected to a maximum acceleration of 2114g in this drop test. The resultant maximum dynamic fracture stress that they experienced was 0.926GPa. The acceleration pulse is below.

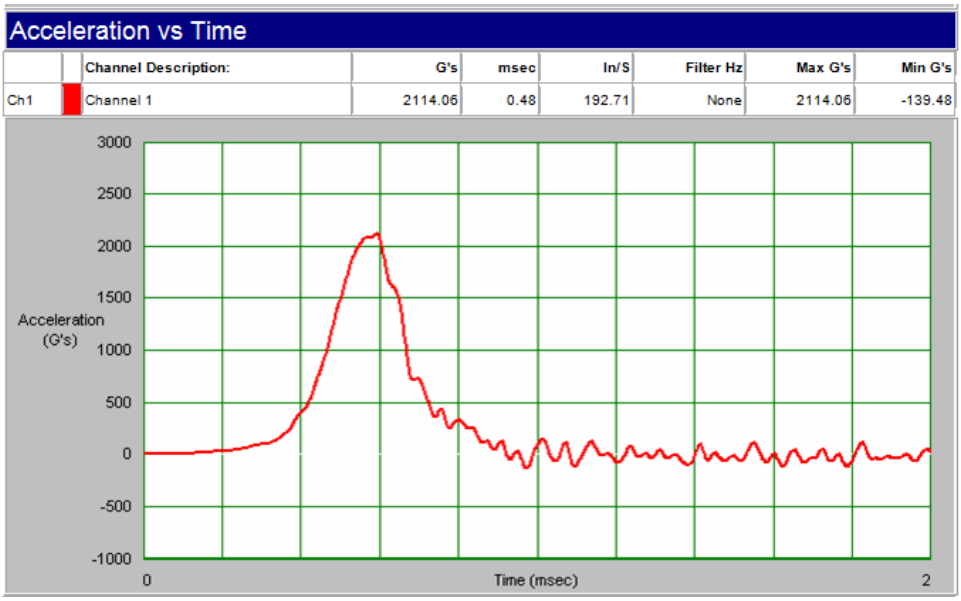

Figure 44. Acceleration Pulse for 2114g drop test

The following images depict the results of this test. Three out of eight functional structures tested were broken.

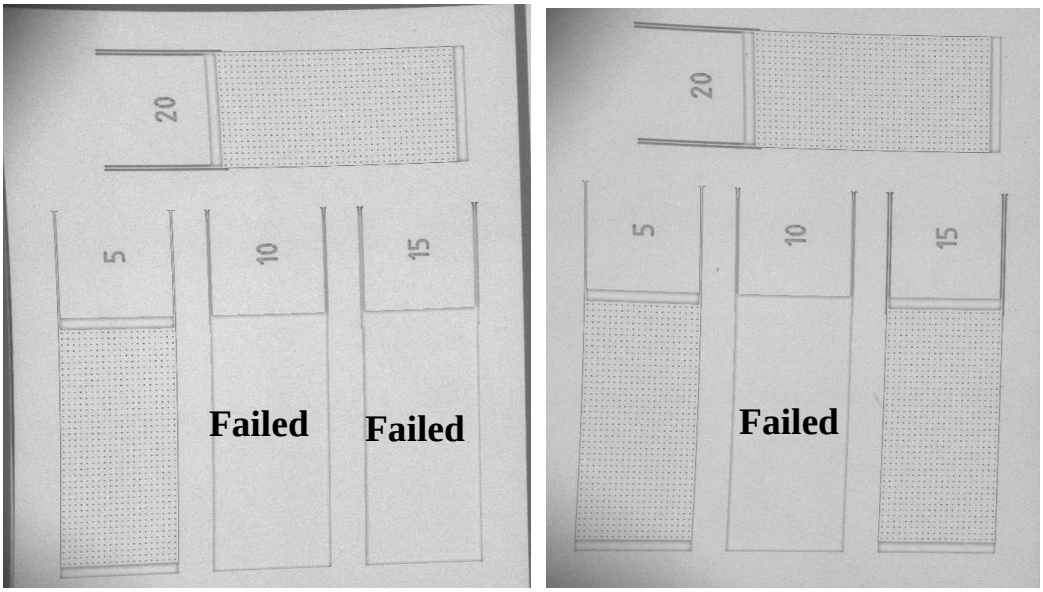

Figure 45. Results from 2114g drop test

2055g Maximum Acceleration Pulse

Eight die were subjected to a maximum acceleration of 2055g in this drop test. The resultant maximum dynamic fracture stress that they experienced was 0.893GPa. The acceleration pulse is shown below.

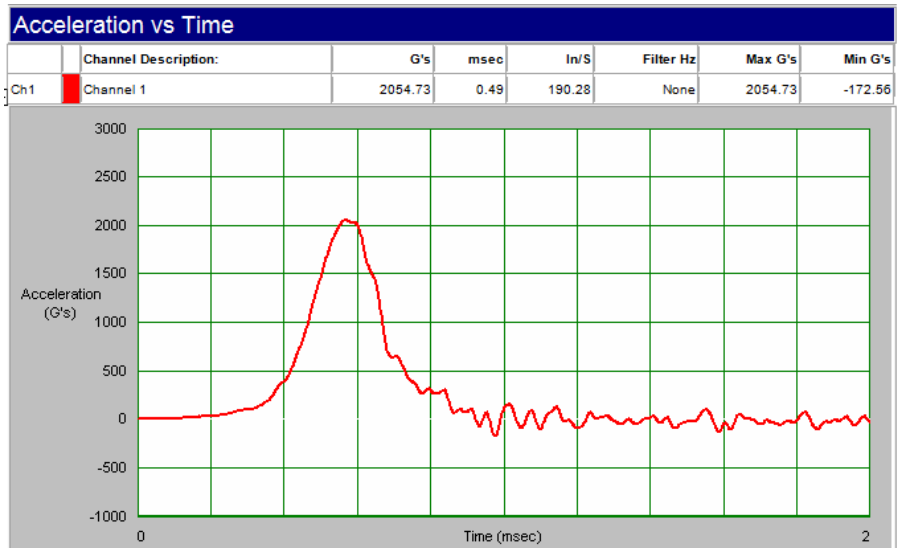

Figure 46. Acceleration Pulse for 2055g drop test

During this test, five out of the eight test structures were broken. This is depicted in the images below.

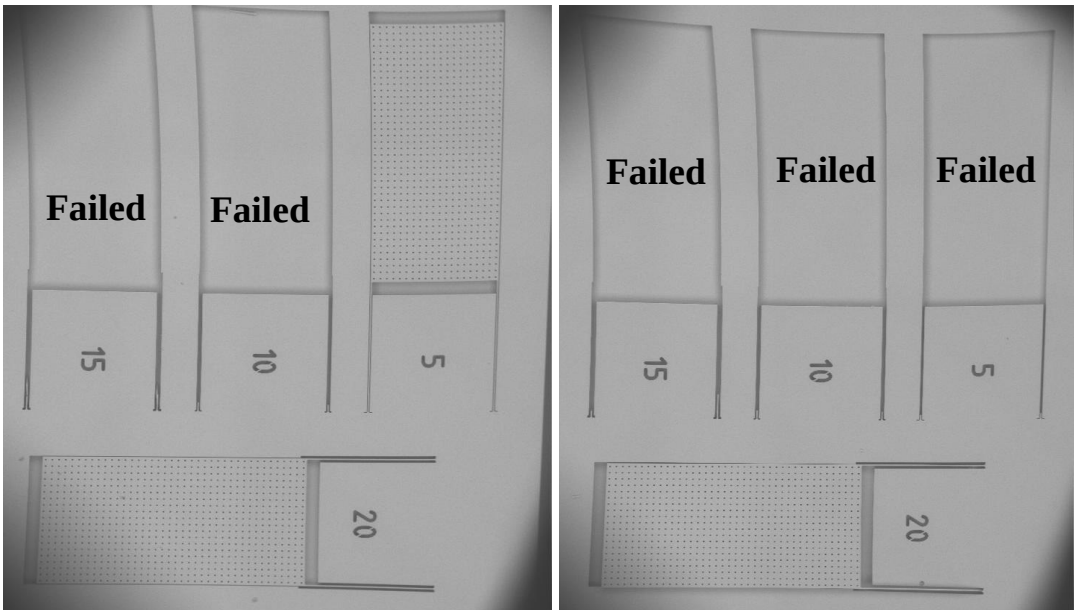

Figure 47. Results from 2055g drop test

Images were also taken of the broken proof masses and fracture sites. These pictures show that, as with the other test structures, failure occurs at the base of the cantilever and along the <111> planes.

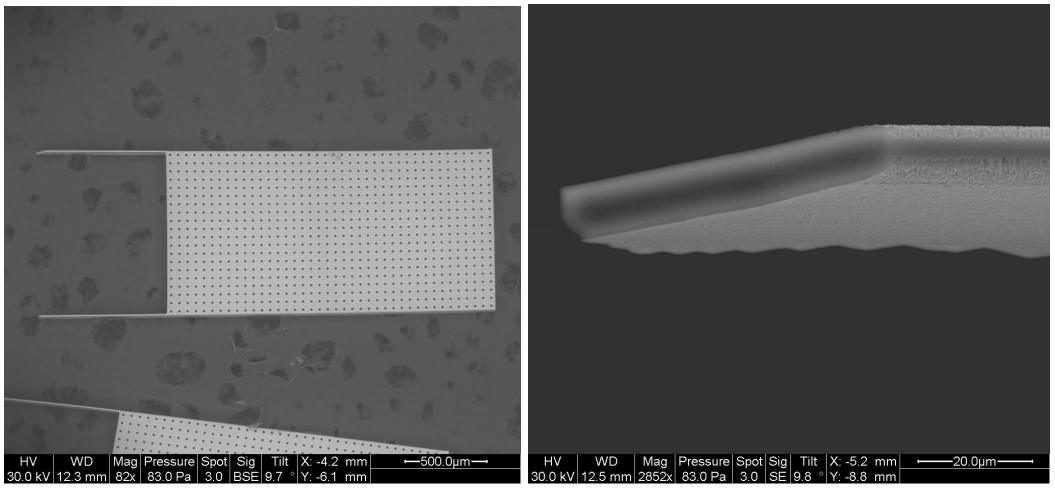

Figure 48. Broken proof mass (left) and fracture site (right) from 2055g test

1636g Maximum Acceleration Pulse

Three die were tested at a maximum acceleration of 1636g. During this test, the die were subjected to a maximum dynamic acceleration of 0.691GPa at the base of their cantilever beams. The figure below shows the acceleration pulse recorded during this test.

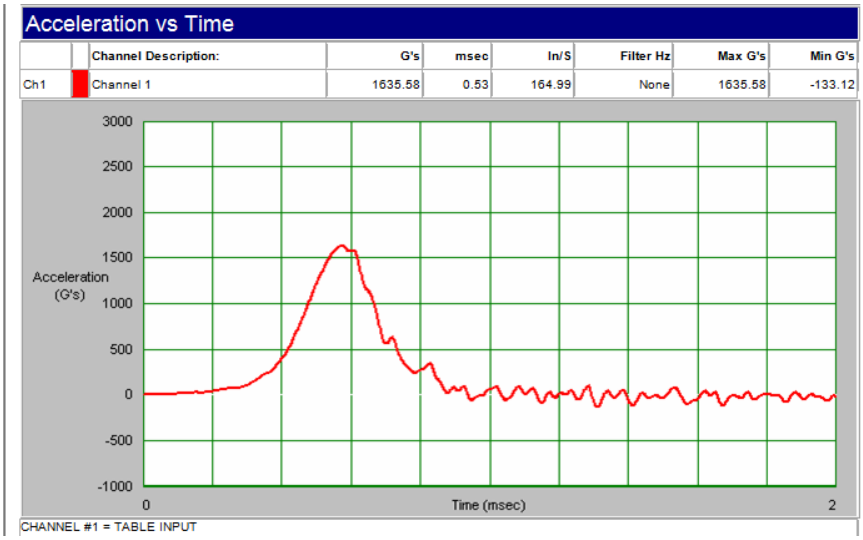

Figure 49. Acceleration Pulse for 1636g drop test

Only three out of the 12 test structures failed during this test. It is interesting to note that all of the 10µm gap devices failed while the other structures remained intact. Images of the failed and unbroken structures are below.

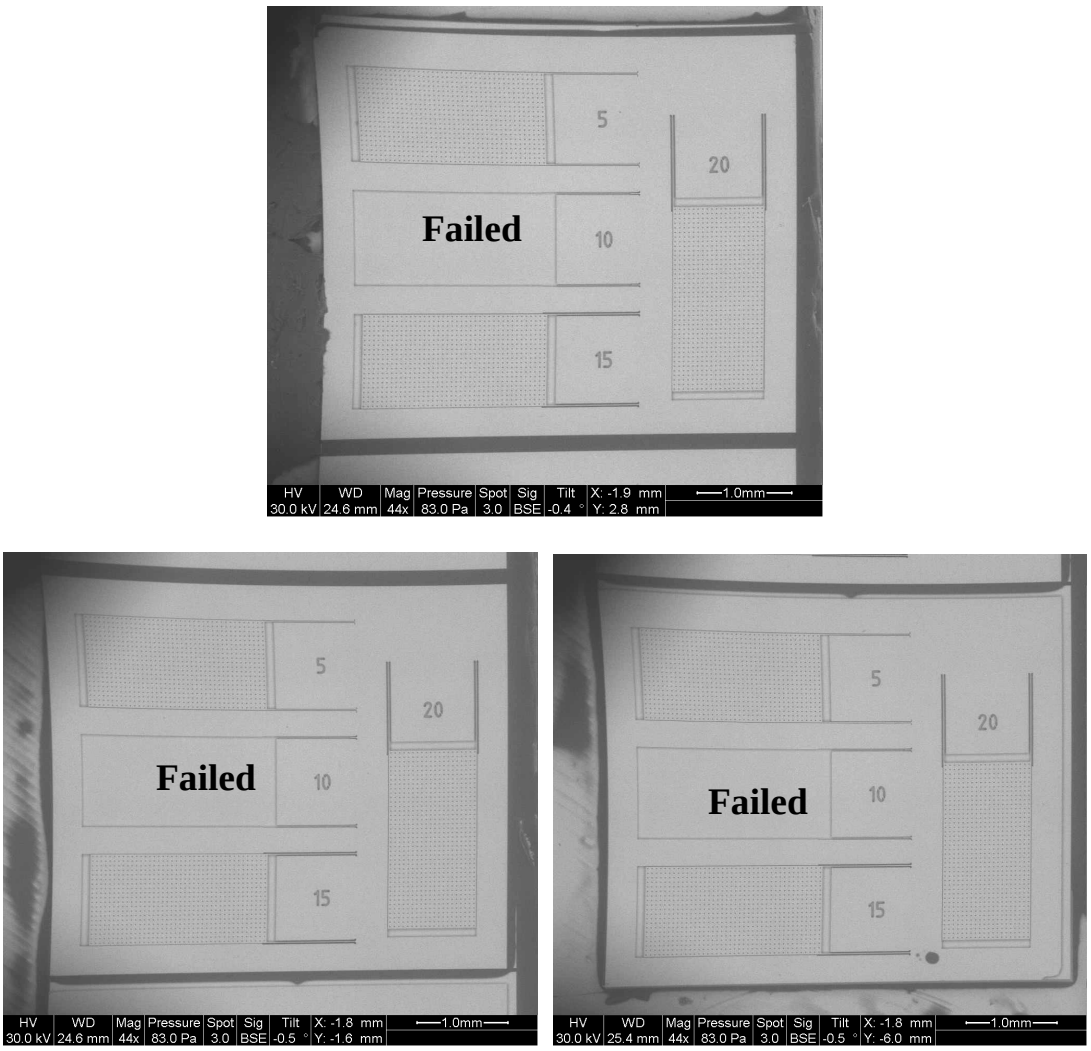

Figure 50. Results from the 1636g drop test

Appendix D

Redesign of in-plane test specimens

The table below represents a redesign option for the in-plane type A devices. In this redesign, the cantilever lengths are unchanged and vary from 100µm to 300µm. The proof mass dimensions, however, are increased considerably from the original test sample size of 750µm x 500µm. The table on the following page shows how the maximum static stress for all sized cantilevers increases when the proof mass is increased to 1000µm x 750µm and then 1250µm x 1000µm. The 5000g acceleration level tests in the table below represent in-plane testing that has already taken place. Note that despite the drop from a 5000g acceleration with the original test structures to a 3000g acceleration with the redesigned structures, the maximum static stress is still increased.

Table 12. Static stress values for redesigned in-plane Type A structures

In-Plane Type A Redesign Information			
Proof Mass Dimensions and (acceleration level)	**Max. Static Stress for 100µm Cantilever (GPa)**	**Max. Static Stress for 200µm Cantilever (GPa)**	**Max. Static Stress for 300µm Cantilever (GPa)**
750µm x 500µm (5000g)	0.29	0.35	0.42
1000µm x 750µm (3000g)	0.44	0.52	0.60
1250µm x 1000µm (3000g)	0.89	1.02	1.14

The image below shows a visual representation of the change in proof mass size that is required to achieve the higher stress values for the in-plane type A devices listed in the table above.

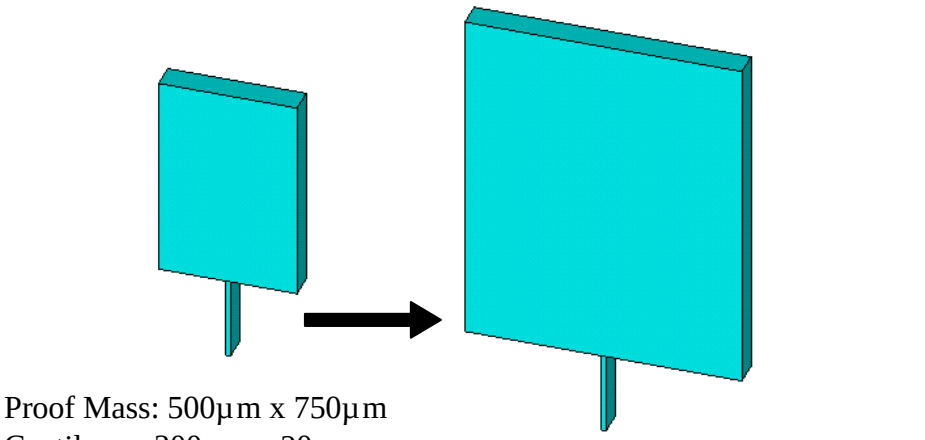

Figure 51. Image demonstrating the proof mass size change required for in-plane type-A devices

Similarly to Table 12 on the previous page, Table 13 represents a redesign option for the in-plane type B devices. In this redesign, the cantilever lengths are unchanged and vary from 100µm to 400µm. The proof mass dimensions, however, are increased considerably from the original test sample size of 400µm x 400µm. The table below shows how the maximum static stress for all sized cantilevers increases when the proof mass is increased to 500µm x 500µm and then 750µm x 750µm. Note that despite the drop from a 5000g acceleration with the original test structures to a 3000g acceleration with the redesigned structures, the maximum static stress is still increased.

Table 13. Static Stress values for in-plane type-B redesigned structures

In-Plane Type B Redesign Information				
Proof Mass Dimensions and (acceleration)	**Max. Static Stress for 100µm Cantilever (GPa)**	**Max. Static Stress for 200µm Cantilever (GPa)**	**Max. Static Stress for 300µm Cantilever (GPa)**	**Max. Static Stress for 400µm Cantilever (GPa)**
400µm x 400µm (5000g)	0.32	0.42	0.53	0.63
500µm x 500µm (3000g)	0.57	0.71	0.85	0.99
750µm x 750µm (3000g)	1.05	1.28	1.50	1.72

The image below shows a visual representation of the change in proof mass size that is required to achieve the higher stress values listed in the table above.

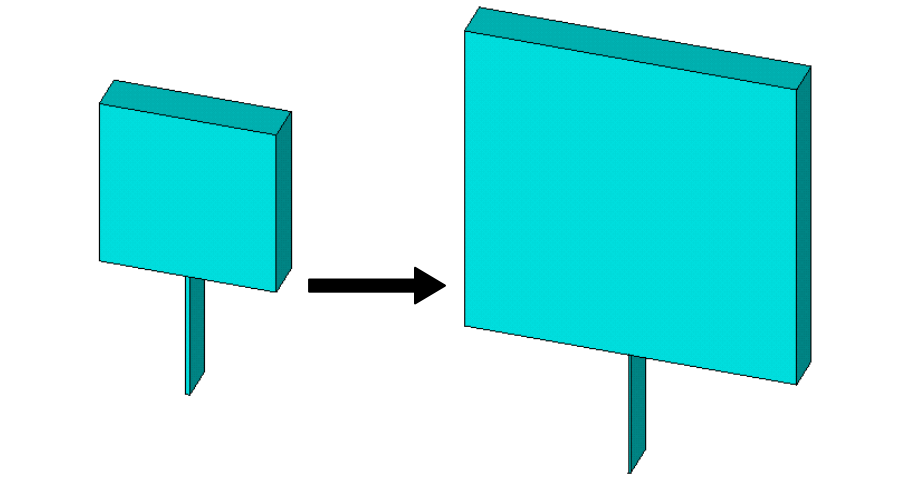

Figure 52. Image demonstrating the proof mass size change required for in-plane type-B devices

Unlike the previous redesign method described in which proof mass size was increased while cantilever length remained fix, the following table demonstrates the effect on maximum static stress when the cantilevers are elongated. Table 14 below shows the effect of a cantilever redesign on the in-plane type-A devices. The 5000g acceleration level tests in the table below represent in-plane testing that has already taken place. As with the previous two redesign examples, the maximum static stress of the redesigned samples is increased despite testing at a 3000g acceleration level instead of a 5000g acceleration level.

Table 14. Static Stress values for in-plane type-A redesigned structures

In-Plane Type A Redesign Information with 750 µm x 500 µm proof mass dimensions	
Cantilever Length and (acceleration level)	**Max. Static Stress (GPa)**
100 (5000g)	0.29
200 (5000g)	0.35
300 (5000g)	0.42
1,000µm (3000g)	0.51
1,200µm (3000g)	0.58
1400µm (3000g)	0.66
1600µm (3000g)	0.73
1800µm (3000g)	0.80
2,000µm (3000g)	0.88
2,200µm (3000g)	0.95

It is interesting to consider the very large increase in cantilever length required to achieve the same maximum stress values that can be achieved through resizing of the proof mass. To put the change in cantilever length in perspective, Figure 53 below shows the transition from an old in-plane device to one of the redesigned in-plane devices.

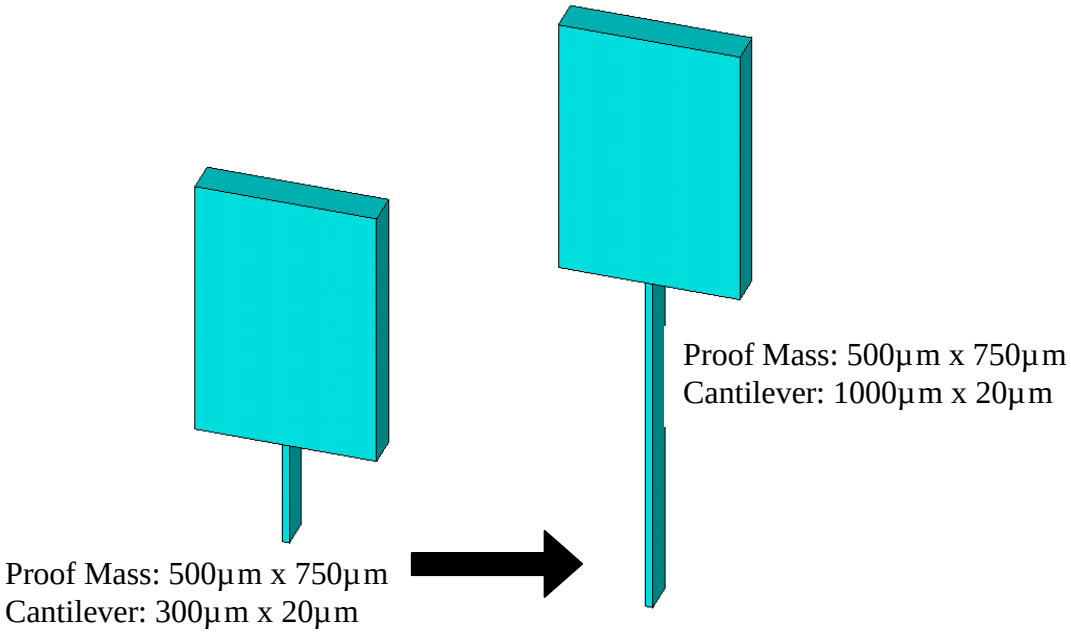

Figure 53. Image demonstrating the cantilever length change required for in-plane type-A devices

As with the in-plane type A devices, an enormous increase in cantilever length is required to increase the static stress values to those found in the proof-mass redesign. Again, the 5000g acceleration level tests in the table below represent in-plane testing that has already taken place. Note that for all of the redesign examples presented, the

maximum static stress of the redesigned samples is increased despite testing at a 3000g acceleration level instead of a 5000g acceleration level.

Table 15. Static Stress values for in-plane type-B redesigned structures

In-Plane Type B Redesign Information with 400µm x 400µm proof mass dimensions	
Cantilever Length and (acceleration level)	**Max. Static Stress (GPa)**
100µm (5000g)	0.32
200µm (5000g)	0.42
300µm (5000g)	0.53
400µm (5000g)	0.63
1,000µm (3000g)	0.44
1,200µm (3000g)	0.88
1,400µm (3000g)	1.01
1600µm (3000g)	1.14
1800µm (3000g)	1.26
2,000µm (3000g)	1.39

An image describing the change in the in-plane type B structures is shown below. This image puts the increased cantilever length in perspective. From examining the dramatic geometry change, it is evident that these redesigned structures will require significantly more are on the silicon die, increasing production cost of test devices.

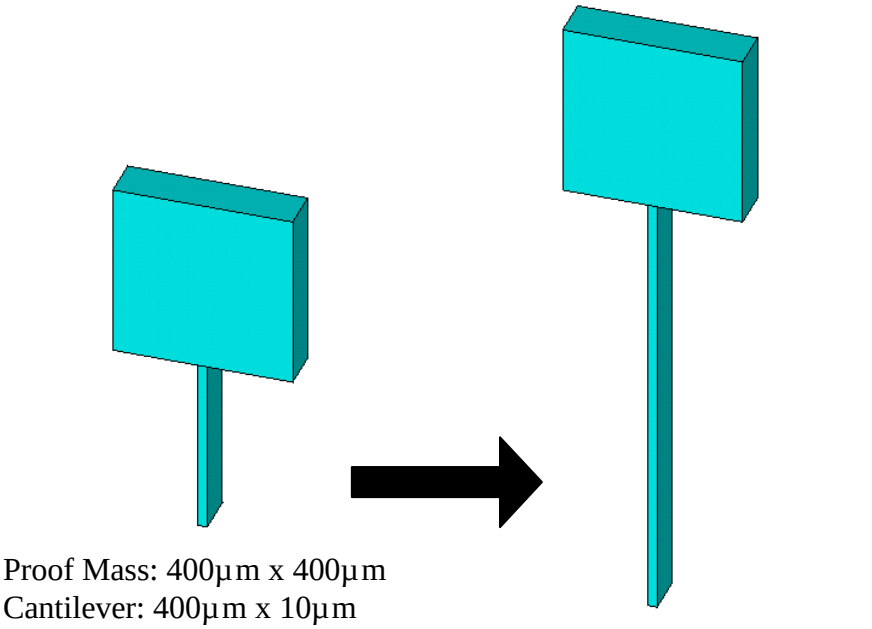

Figure 54. Image demonstrating the cantilever length change required for in-plane type-B devices

Works Cited

[1] “Global MEMS/Microsystems markets and opportunities.” Small Times: Micro and Nanotech Manufacturing, Tools and Materials. Penn Well. September 2008. http://www.smalltimes.com/worldinbriefs/special_feature.cfm

[2] Lall, P., Panchagade, D., et al. “Failure-Envelope Approach to Modeling Shock and Vibration Survivability of Electronic and MEMS Packaging.” Electronic Components and Technology Conference, 2005. Proceedings. 55th. May 31 2005-June 3 2005. 480-490.

[3] Taechung, Y. and Kim, C. “Measurement of mechanical properties for MEMS materials.” Measurement Science & Technology, 10, pp. 706-716.

[4] Wilson, C. and Beck, A. Fracture testing of bulk silicon microcantilever beam subjected to a side load. Journal of Microelectromechanical Systems. 5 (1996) 142-50.

[5] Fujii, T. and Akiniwa, J. “Molecular dynamics analysis for fracture behavior of single crystal silicon thin film with micro notch.” Modelling and Simulation in Materials Science and Engineering. 14 (2006) S73-S83.

[6] Nemeth, N., et al. “Probabalistic Fracture Strength of High-Aspect-Ratio Silicon Carbide Microspecimens Predicted.” NASA Glenn Research Center. 2005 Research and Technology Update.

[7] Yi, T., Li, L., and Kim, C. J., 2000, “Microscale material testing of single crystal silicon: process effects on surface morphology and tensile strength,” Sensors and Actuators A: Physical, 83, pp. 172-178.

[8] Namazu, T., Isono, Y., and Tanaka, T., 2000, “Evaluation of Size Effect on Mechanical Properties of Single Crystal Silicon by Nanoscale Bending Test Using AFM”, IEEE Journal of Microelectromechanical Systems, 9(4), pp. 450-459.

[9] Namazu, T., Isono, Y., and Tanaka, T., 2000, “Nano-Scale Bending Test of Si Beam for MEMS”, Proceedings of IEEE Thirteenth Annual Int. Conf. on Micro Electro Mechanical Systems, Miyazaki, Japan, pp. 205-210.

[10] Hu, S. M., 1982, “Critical stress in silicon brittle fracture, and effect of ion implantation and other surface treatments,” Journal of Applied Physics, 53 (5), pp. 3576-3580.

[11] Chen, K., Ayon, A., and Spearing, S. M., 2000, “Controlling and Testing the Fracture Strength of Silicon on the Mesoscale,” Journal of American Ceramic Society, 83(6), pp. 1476-1484.

[12] Suwito, W., Dunn, M. L., Cunningham, S. J., and Read, D. T., 1999, “Elastic moduli, strength, and fracture initiation at sharp notches in etched single crystal silicon microstructures,” Journal of Applied Physics, 85(7), pp. 3519-3534.

[13] Lehmann, G., Lomonosov, A. M., Hess, P., and Gumbsch, P., 2003, “Impulsive fracture of fused quartz and silicon crystals by nonlinear surface acoustic waves,” Journal of Applied Physics, 94(5), pp. 2907-2914.

[14] Hasin, S. “Test Methodologies for Dynamic Fracture Strength of Single Crystal Silicon,” Master of Science Thesis. 2008. University of Maryland Department of Mechanical Engineering.

[15] Balachandran, B., and Magrab, E., 2004, *Vibrations*, Thomson, Belmont, CA

[16] EPO-TEK 353ND Technical Data Sheet. Epoxy Technology. September, 2008. < http://www.epotek.com/SSCDocs/datasheets/353ND.PDF>

[17] Model 350B23 ICP Accelerometer Installation and Operating Manual. PCB Piezotronics Vibration Divison. Pg. 3.

[18] Sloan, J. L., 1985, *Design and Packaging of Electronic Equipment*, Van Nostrand Reinhold Company, New York, NY, pp.430-432

[19] Dave Hopkins, Army ARL

[20] Askeland, D. R., 1984, *The Science and Engineering of Materials*, Brooks/Cole Engineering Division, Wadsworth, Inc., Belmont, CA, pp.56-65.